



Science Arts & Métiers (SAM)

is an open access repository that collects the work of Arts et Métiers Institute of Technology researchers and makes it freely available over the web where possible.

This is an author-deposited version published in: <https://sam.ensam.eu>
Handle ID: <http://hdl.handle.net/10985/8644>

To cite this version :

Frédéric ALIZARD, Jean-Christophe ROBINET, Xavier GLOERFELT - A domain decomposition matrix-free method for global linear stability - Computers & Fluids - Vol. 66, p.63-84 - 2012

Any correspondence concerning this service should be sent to the repository

Administrator : scienceouverte@ensam.eu



A Domain Decomposition Matrix-Free Method for Global Linear Stability

ALIZARD Frédéric ⁺, ROBINET Jean-Christophe ^{*}, GLOERFELT Xavier

^{*}

⁺ *Laboratoire DynFluid-CNAM Paris, 15, rue Marat 78210 Saint-Cyr l'Ecole. France.*

^{*} *Laboratoire DynFluid-ENSAM Paris, 151 Boulevard de l'Hôpital 75013 Paris. France.*

Abstract

This work is dedicated to present a matrix-free method for global linear stability analysis in geometries composed of multi-connected rectangular subdomains.

An Arnoldi technique based on snapshots in subdomains of the entire geometry combined with a multidomains linearized DNS based on an influence matrix with respect to finite difference schemes is adopted and illustrated on three benchmark problems: the lid-driven cavity, the square cylinder and the open cavity flow.

The efficiency of the method to extract large scale structures in a multidomains framework is emphasized. Such a method appears thus a promising tool to deal with large computational domains and three-dimensionality within a parallel architecture.

Email address: corresponding author: `frederic.alizard@cnam.fr` (ALIZARD Frédéric ⁺)

Notations

In this section, the notations used for domains decomposition method are given below:

- \mathcal{D} is the computational domain.
- $\partial\mathcal{D}$ is the boundary of \mathcal{D} .
- N_b denotes the number of subdomains which composes \mathcal{D}
- $\{\mathcal{D}_p\}_{p=1, N_b}$ is a partition of \mathcal{D} .
- $\partial\mathcal{D}_i$ denotes the boundary of \mathcal{D}_i .
- \mathcal{I}_i is the union of all the interfaces of the subdomain \mathcal{D}_i .
- N_i : number of nodes of the interface \mathcal{I}_i .
- $\{\gamma_{i,j}\}_{j=1, N_i}$ references the nodes of \mathcal{I}_i .
- χ_i represents the boundary except the interface of the subdomain \mathcal{D}_i :
 $\chi_i = \partial\mathcal{D}_i \setminus \mathcal{I}_i$
- $N_{\mathcal{I}}$: number of interfaces

1. Introduction

Many open flows exhibit a wide range of space and time scales. In several situations, they are characterized by dynamically dominant large-scale structures. For instance, structures of wakes, jets and shear layers are dominated by vortices with characteristic recurrent form that are commonly called coherent structures. Hence, a physical understanding of their relative role they play in the flow dynamics is of crucial interest to the description of mass, momentum and heat transport. In this context, several attempts were dedicated to bring new elements in describing complex open flow dynamics through coherent structures. Among various modelling of such structures, global modes technique based on the knowledge of disturbances behaviour about a basic state appears as a fundamental framework and has been intensively studied these last years (see Theofilis (2003) and Theofilis (2011) for a detailed review). Nonetheless, the accurate description of disturbance behaviour in complex geometries remains a challenging task. One may precise

that global modes are associated with eigenmodes of the Jacobian matrix about a basic state with respect to the Navier-Stokes operator. From those analyses, one may distinguish between matrix and matrix-free methods. The common point of each of them is the evaluation of the action of the Jacobian matrix on perturbation fields. The first strategy requires solving a large eigenvalue problem (EVP) through the so-called global stability equations. Such a task necessitates the discretization and the construction of the EVP in a matrix form as well as its storage. On one hand, the elliptic nature of the problem implies employing appropriate boundary conditions in a Fourier space. This last point may yield some difficulties in correctly dissipating convective waves along the boundaries. In this context, Ehrenstein and Gallaire (2005) introduced a convective boundary condition using a Gaster transformation about a circular frequency, under the assumption of a parallel flow at the outflow. Therefore, such a boundary condition is restricted to a small range of circular frequencies. By contrast, within a DNS framework, the convective velocity of the perturbation reaching the outlet may be updated at each time step allowing disturbances to exit smoothly out of the domain (see for instance Pauley et al. (1990)). On the other hand, although the matrix method has been used successfully in several cases, (see Theofilis (2003) or Åkervik et al. (2007) for instance) the storage of the discretized global stability equations still poses a great computational challenge due to its very large dimension (see Bagheri et al. (2009a)). Recently, Rodriguez and Theofilis (2009) proposed a methodology based on a massively parallel solution. Nevertheless, it demanded a very large storage requirement which can be treated only on supercomputing cluster. To overcome this difficulty, Merle et al. (2010) presented an alternative in which EVP is discretized using an high-order finite-difference scheme. The technique involving sparse matrices exhibits a significant reduction in memory requirement. However, the authors outlined the numerical difficulty in properly describing propagative waves in open flows. They have suggested that poor conditioning of discretized matrices, which is closely associated with non-normality, and boundary conditions constituted an inherent difficulty of such a method. Finally, a multidomains method is also presented recently by De Vicente et al. (2011). Nevertheless, this technique solely focused on closed cavity flows of various rectangular multi-connected subdomains geometries and not on open flows.

The key concept behind the matrix-free method is to use explicit evaluation of action of the Jacobian matrix on a perturbation field via a time-

stepping method. A set of disturbances fields that spans a small Krylov subspace is generated by a numerical simulation of the linearized Navier-Stokes equations. Global modes are thus extracted from the resulting data sequence. The Arnoldi algorithm based on an orthonormalization of the Krylov subspace is particularly successful in this respect. The method was popularized fifteen years ago for the analysis of bifurcations with regards to confined flows by Edwards et al. (1994). This approach based on snapshots of the velocity fields has not only the benefit to use an existing Direct Numerical Simulation (referenced as DNS hereafter) code but also to provide a unified code for a wide variety of complex flows. In the past decades, several studies relying on such a methodology have been dedicated to analyze diverse kinds of both closed and open flows. Among these, we can point out the work of Barkley and Henderson (1996) in which the authors identified the second linear instability underlying the two-dimensional Von Karman vortex street associated with a circular cylinder. A Floquet theory related to snapshots of the linearized DNS about a periodic flow using spectral elements discretization is used. By means of a similar numerical method, Barkley et al. (2002) emphasized the emergence of unsteadiness and three-dimensionality with respect to a flow over a backward-facing step. Recently, this strategy seems to become increasingly popular and a promising tool under a global stability framework according to three-dimensionality, complex geometries and complex flows. In this context, the first attempt to deal with three-dimensional flow in an incompressible regime was carried out by Tezuka and Kojiro (2006). The authors revealed the appearance of nonoscillatory global modes according to a flow around a spheroid body using snapshots performed on a non linearized DNS with the Chiba method (see Chiba (1998)). Two types of initial values about the steady flow is thus used to initialize the DNS in order to recover the dynamics of a small perturbation. More recently, Bagheri et al. (2009b) investigated the self-sustained global oscillations in a three-dimensional incompressible jet in cross-flow. Snapshots of perturbation velocity fields relying on linearized DNS discretized by a Fourier-Chebyshev spectral method allows to identify both high- and low-frequency unstable global modes associated with shear-layer instabilities and shedding vortices in the wake of the jet respectively. Finally, Bres and Colonius (2008) identified the occurrence of three-dimensional patterns with respect to two-dimensional flow over a rectangular cavity at low-Reynolds numbers as unstable global eigenmodes. A compressible linearized DNS solver based on sixth-order compact finite-difference scheme in the inhomogeneous plane in combination with a Fourier

expansion in the spanwise direction is employed. In a similar way, Mack and Schmid (2011) showed new results regarding the flow dynamics of a swept flow around a parabolic body in a compressible regime. A large variety of global modes is highlighted as boundary-layer and acoustic modes.

From the above discussion, it is clear that understanding of open flow dynamics through global modes could greatly benefit from the development of efficient Navier-Stokes solvers devoted to large computational domains and three-dimensionality. In this context, matrix-free methods appears to be an appropriate choice. Nevertheless, their main drawback lies in two major facts. In one hand, it necessitates several time-integration of linearized DNS which is time consuming, in particular when dealing with low frequency unsteadiness. On the other hand, both the storage of snapshots and Krylov methods related to large computational domains, fine spatial discretization and three-dimensionality may yield difficulties in terms of memory requirement and time spending of the eigenmodes algorithm. To overcome these limitations, domain decomposition methods in which the geometry is decomposed into subdomains, combined with parallel architectures seems to be an appropriate choice. For that purpose, this work is motivated by developing and validating a time-stepping global stability method based on a multidomains solver according to the linearized DNS in combination with an Arnoldi algorithm associated with snapshots of each subdomain which composes the full geometry.

Regarding the linearized DNS solver, one may remark that continuity influence matrix technique combined with a connectivity table has been rather successful to handle communications between each subdomain. In particular, this method has been popularized within a spectral discretization framework by Sabbah and Pasquetti (1998) and Raspo (2003) and recently within high-order finite-difference scheme framework by Abide and Viazzi (2005) and Alizard et al. (2010b). In particular, both last authors have pointed out that it constitutes an accurate and robust technique for dealing with multi-connected rectangular subdomains and leads to well conditioning continuity influence matrix. Hence, multidomains incompressible DNS and linearized DNS codes written in primitive variables with respect to sixth-order compact finite-difference scheme defined in a fully staggered grid are chosen in the present paper.

Concerning Krylov technique, Schmid (2010) outlined recently the possibility to focus on regions of the perturbation velocity fields where dynamics is relevant. By considering that the global unsteadiness is felt all over the

flow field, it seems thus interesting to further explore this concept by solely focusing on snapshots of subdomains in order to reconstruct the perturbation fields associated with the full geometry.

Therefore, the technique proposed in this manuscript raises two fundamental questions. On one hand, does the partitioning has an influence on global eigenmodes derived from snapshots of the linearized DNS performed on the entire flow fields ? On the other hand, informations extracted only from subdomains are sufficient to recover the global eigenmodes on the entire flow field ?

In order to give an answer to latters, the paper is organized as follows. First, the numerical method dealing with multidomains approach is described for both the Navier-Stokes solver and the global linear stability. Then, numerical experiments will be devoted to illustrate these two aspects. On one hand, we will focus on emphasizing that the partitioning has no significant influence on the global modes spatial accuracy with respect to geometry composed of multi-connected rectangular subdomains. On the other hand, we will attempt to highlight that snapshots performed on subdomains derived from the linearized DNS could be used independently to assess the linear dynamics of the full geometry. To illustrate these affirmations, three cases will be studied: the closed flow with regards to a lid-driven cavity, and flows which past over a square cylinder and a generic open cavity. The interest of the latter is distinguished in the occurrence of several space and time scales and localized instability regions.

2. Direct numerical simulation

2.1. Single domain approach

The non-dimensionalized governing equations for an incompressible flow are given by:

$$\begin{cases} \frac{\partial \mathbf{u}}{\partial t} + (\mathbf{u} \cdot \nabla) \mathbf{u} = -\nabla p + \frac{1}{\text{Re}} \nabla^2 \mathbf{u} \\ \nabla \cdot \mathbf{u} = 0 \end{cases} \quad (1)$$

with $\mathbf{u}(\mathbf{x}, t)$ and $p(\mathbf{x}, t)$, the velocity vector and the pressure field respectively. Re denotes the Reynolds number. Temporal integration of (1) is based on a semi-implicit fractional-step scheme. The nonlinear terms are recast in a conservative form and advanced in time with an explicit third-order Adams-Bashforth scheme. The viscous terms are integrated via an

implicit Crank-Nicolson scheme. A projection method described by Armfield and Street (2003) and Brown et al. (2001) is employed to ensure the divergence-free condition. A provisional velocity field \mathbf{u}^* is then determined by solving:

$$\left\{ \begin{array}{l} \frac{\mathbf{u}^* - \mathbf{u}^n}{\Delta t} + [(\mathbf{u} \cdot \nabla) \mathbf{u}]^{n+\frac{1}{2}} = -\nabla p^{n+\frac{1}{2}} + \frac{1}{Re} \nabla^2 \left(\frac{\mathbf{u}^* + \mathbf{u}^n}{2} \right) \\ [(\mathbf{u} \cdot \nabla) \mathbf{u}]^{n+\frac{1}{2}} = \sum_{j=1}^3 \beta_j \mathcal{N}(u^{n+1-j}) \\ \text{with } \{\beta_{j=1,3}\} = \{23/12, -16/12, 5/12\} \end{array} \right. \quad (2)$$

where \mathcal{N} is the nonlinear operator. Then, a correction is completed by introducing ϕ which satisfies the following Poisson equation:

$$\left\{ \begin{array}{l} \nabla \cdot \mathbf{u}^{n+1} = 0 \implies \Delta \phi^{n+1} = \frac{\nabla \cdot \mathbf{u}^*}{\Delta t} \\ \left. \frac{\partial \phi^{n+1}}{\partial n} \right|_{\partial \mathcal{D}} = 0 \end{array} \right. \quad (3)$$

Therefore, the corrected divergence-free velocity field at the step $n + 1$ is given by:

$$\mathbf{u}^{n+1} = \mathbf{u}^* - \Delta t \nabla \phi^{n+1} \quad (4)$$

The pressure is updated in the final stage:

$$p^{n+\frac{1}{2}} = p^{n-\frac{1}{2}} + \phi^{n+1} - \frac{\Delta t}{2Re} \Delta \phi^{n+1} \quad (5)$$

where the third term in the right-hand side is used to ensure second-order accuracy in time for the pressure (Brown et al., 2001)

The variable arrangement used is the standard MAC staggered Cartesian grid as depicted in Figure 1 requiring an interpolation between node and center grid points. This crucial step is realized through a sixth-order Lagrange interpolation. The spanwise direction z is discretized with a Fourier collocation. The three-dimensional problem is then reduced to a series of two-dimensional ones with respect to each spanwise wave number.

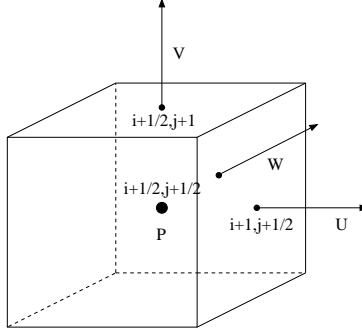


Figure 1: The standard MAC staggered Cartesian grid is depicted. U , V , W are the streamwise, normal, and spanwise velocity components respectively, P is the pressure. The coordinate system is referenced as (x, y, z) . x , y , and z are oriented in the streamwise, vertical, and spanwise directions respectively. The coordinates of centers and faces in (x, y) -plane are also shown.

Spatial discretization of nonlinear terms in the (x, y) -plane are accomplished with a sixth-order compact finite-difference scheme based on staggered arrangement as shown in Figure 2. Compact approximations for the staggered grid have been introduced by Chang and Shiner (1985) and extended to high order by Lele (1992). For convenience and without lack of generality, only the one-dimensional case is considered. here, the approximations of the first derivative, denoted by f' , on centers of the cells are realized through:

$$\alpha_1^i f'_{i-1} + f'_i + \alpha_2^i f'_{i+1} = a_1^i f_{i-3/2} + a_2^i f_{i-1/2} + a_3^i f_{i+1/2} + a_4^i f_{i+3/2} \quad (6)$$

The generalization of this compact finite-difference scheme to non uniform grid can be achieved either by using transformed co-ordinates, or by integrating directly the metrics in the computation of the coefficients. Gamet et al. (1999) have shown that the second technique can reduce numerical errors. This method has first been used to define fourth-order compact scheme for nonuniform grids by Goedheer and Potters (1985). Truncated Taylor series of f and f' defined on the stretched grid are used to determine the coefficients of the scheme based on the desired accuracy, resulting in the computation of different sets of coefficients for each grid point (indicated by the superscript i of the coefficients in (6)). The technique is simply extended to a staggered

arrangement, yielding the matrix system:

$$X\mathbf{a} = \mathbf{b} \quad \text{with} \quad \mathbf{a} = \begin{pmatrix} \alpha_1^i \\ \alpha_2^i \\ a_1^i \\ a_2^i \\ a_3^i \\ a_4^i \end{pmatrix} \quad \text{and} \quad \mathbf{b} = \begin{pmatrix} 0 \\ 1 \\ 0 \\ 0 \\ 0 \\ 0 \end{pmatrix}$$

$$X = \begin{pmatrix} 0 & 0 & 1 & 1 & 1 & 1 \\ -1 & -1 & X_{i-3/2} & X_{i-1/2} & X_{i+1/2} & X_{i+3/2} \\ -X_{i-1} & -X_{i+1} & X_{i-3/2}^2/2 & X_{i-1/2}^2/2 & X_{i+1/2}^2/2 & X_{i+3/2}^2/2 \\ -X_{i-1}^2/2 & -X_{i+1}^2/2 & X_{i-3/2}^3/6 & X_{i-1/2}^3/6 & X_{i+1/2}^3/6 & X_{i+3/2}^3/6 \\ -X_{i-1}^3/6 & -X_{i+1}^3/6 & X_{i-3/2}^4/24 & X_{i-1/2}^4/24 & X_{i+1/2}^4/24 & X_{i+3/2}^4/24 \\ -X_{i-1}^4/24 & -X_{i+1}^4/24 & X_{i-3/2}^5/120 & X_{i-1/2}^5/120 & X_{i+1/2}^5/120 & X_{i+3/2}^5/120 \end{pmatrix}$$

where we have noted $X_\alpha = x_\alpha - x_i$. The matrix inversion are performed once prior to calculations. The final scheme will reduce to the sixth-order compact approximation in the case of a uniformly spaced grid. For sufficiently smooth grids (as considered in the present study), the high-accuracy is preserved, and there is no conditioning problem in the matrix inversions, based on standard LU-decomposition. The method is extended in a straightforward way for the evaluation of the first derivative on the nodes as:

$$\kappa_1^i f'_{i-1/2} + f'_{i+1/2} + \kappa_2^i f'_{i+3/2} = b_1^i f_{i-1} + b_2^i f_i + b_3^i f_{i+1} + b_4^i f_{i+2} \quad (7)$$

Along the boundaries, the systems arising from (6) and (7) are closed by explicit fourth-order schemes with respect to a staggered point distribution:

$$\begin{cases} f'_N &= c_{N-1/2} f_{N-1/2} + c_{N-3/2} f_{N-3/2} + c_{N-5/2} f_{N-5/2} + c_{N-7/2} f_{N-7/2} \\ f'_1 &= c_{1/2} f_{1/2} + c_{3/2} f_{3/2} + c_{5/2} f_{5/2} + c_{7/2} f_{7/2} \\ f'_{N-1/2} &= c_N f_N + c_{N-1} f_{N-1} + c_{N-2} f_{N-2} + c_{N-3} f_{N-3} \\ f'_{1/2} &= c_0 f_0 + c_1 f_1 + c_2 f_2 + c_3 f_3 \end{cases} \quad (8)$$

The formulation is easily generalized in a three-dimensional configuration by considering the variable arrangement shown in Figure 1.

Viscous terms are discretized with second-order accuracy in space with respect to Taylor series expansion formulated on a non-staggered grid. As a consequence, the semi-implicit scheme (2) as well as the pressure correction (3) yield linear algebraic systems composed of tridiagonal block matrices.

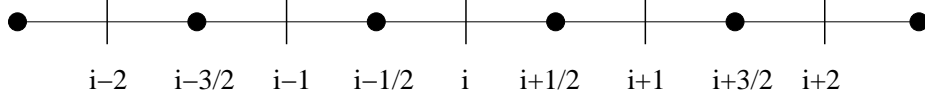


Figure 2: The centers (filled circles) and nodes (vertical lines) in the grid arrangement are illustrated.

In the present work, a direct solver based on a block version of Thomas' algorithm is employed to solve Helmholtz and Poisson problems. The first step is performed in a preprocessing stage allowing a fast resolution at each time-step. Validations are shown in Appendix A.

In our cases, only two-dimensional base flow and two- or three-dimensional periodic perturbations will be explored.

2.2. Domain decomposition: Continuity Influence Matrix method

2.2.1. Continuous formulation

The projection method reduces the time discretized Navier-Stokes equations into a set of Helmholtz and Poisson-Neumann problems. As discussed by Abide and Viazzo (2005) recently, an efficient way to solve these problems within a multidomains framework is the continuity influence matrix strategy. This technique has been extensively applied using spectral method to deal with pressure boundary condition by Kleiser and Schumann (1980), Tuckerman (1989), vorticity wall condition by Daube (1992), and interfaces in a multidomains framework (see Sabbah and Pasquetti (1998) and Raspo (2003)). A detailed review is given by Peyret (2002).

For that purpose, the solution on the complete domain \mathcal{D} is decomposed into a set of N_b sub-problems on a non-overlapped partition $(\mathcal{D}_k)_{k=1, N_b}$ of \mathcal{D} . The problems are coupled with the so-called transmission conditions through the continuity of the variables and their normal derivatives across interfaces between each subdomain. For convenience, let us consider the Poisson-Neumann problem. A trivial modification yields a formulation with respect to the Helmholtz problem. The transmission condition may be written as:

$$\frac{\partial \phi_i}{\partial n}(\gamma_{ip}) = \frac{\partial \phi_j}{\partial n}(\gamma_{jp}) \quad \text{and} \quad \phi_i(\gamma_{ip}) = \phi_j(\gamma_{jp}) \quad \text{for} \quad \gamma_{ip} = \gamma_{jp} \in \mathcal{I}_i \cap \mathcal{I}_j \quad (9)$$

with n the normal across the interface between \mathcal{D}_i and \mathcal{D}_j (see Figure 3). A

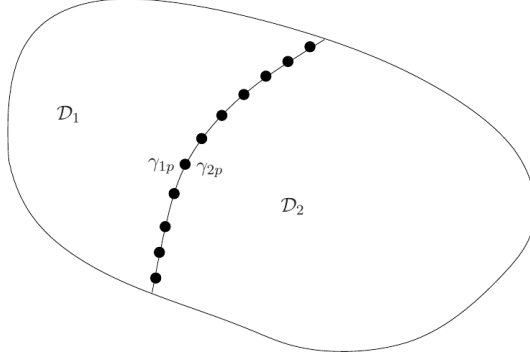


Figure 3: The decomposition of \mathcal{D} into the partition formed by $\mathcal{D}_1 \cup \mathcal{D}_2$ is illustrated.

solution to the linear problem, is searched as the following linear combination:

$$\begin{aligned}\phi_i &= \tilde{\phi}_i + \sum_{k=1}^{N_i} \lambda_{ik} \bar{\phi}_{ik} \text{ in } \mathcal{D}_i \\ \lambda_{ik} &= \phi_i(\gamma_{ik}) \text{ for } \gamma_{ik} \in \mathcal{T}_i.\end{aligned}\tag{10}$$

where $\tilde{\phi}_i$ and $\bar{\phi}_{ik}$ are the solution of $N_b + 1$ problems referenced as \mathcal{P}_1 and \mathcal{P}_k with $k=(1, N_b)$ respectively:

$$\mathcal{P}_1 : \begin{cases} \Delta \tilde{\phi}_i = S|_{\mathcal{D}_i} \text{ in } \mathcal{D}_i \\ \tilde{\phi}_i = \phi_i|_{\chi_i} \text{ on } \chi_i \\ \tilde{\phi}_i = 0 \text{ on } \mathcal{T}_i \end{cases}\tag{11}$$

$$\mathcal{P}_k : \begin{cases} \Delta \bar{\phi}_{ik} = 0 \text{ in } \mathcal{D}_i \\ \bar{\phi}_{ik} = 0 \text{ on } \chi_i \\ \bar{\phi}_{ik} = \delta_{ik} \text{ for } \gamma_{ik} \in \mathcal{T}_i \end{cases}\tag{12}$$

where δ_{ip} is the Kronecker symbol and S the right member of the Poisson equation derived from (3).

The continuity of the normal derivative across the interface yields to the following equation:

$$\frac{\partial \tilde{\phi}_i}{\partial n}(\gamma_{ip}) - \frac{\partial \tilde{\phi}_j}{\partial n}(\gamma_{jp}) = \sum_{k=1}^{N_j} \lambda_{jk} \frac{\partial \bar{\phi}_{jk}}{\partial n}(\gamma_{jp}) - \sum_{k=1}^{N_i} \lambda_{ik} \frac{\partial \bar{\phi}_{ik}}{\partial n}(\gamma_{ip})\tag{13}$$

with $\gamma_{ip} = \gamma_{jp} \in \Upsilon_i \cap \Upsilon_j$ interface values between domains i and j . Equation (13) applied to each interface may be recast in a linear system:

$$\mathcal{M}\Sigma = \mathcal{H} \quad \text{with} \quad \Sigma = \begin{pmatrix} \lambda_{11} \\ \dots \\ \lambda_{1N_1} \\ \dots \\ \lambda_{jN_j} \\ \dots \\ \lambda_{N_T N_{N_T}} \end{pmatrix} \quad \text{and} \quad \mathcal{H} \text{ the left member provided by 13} \quad (14)$$

where \mathcal{M} is the so-called continuity influence matrix. The resolution of (14) provides thus discrete values of the N_T interfaces. The next part is devoted to emphasize how this theoretical framework is employed with a staggered finite difference scheme.

2.2.2. Discrete formulation

For convenience, we focus only on the one-dimensional case. The domain \mathcal{D} is split into two subdomains. The extension to the three-dimensional case is easily conducted by considering the variables distribution in Figure 1. A difficulty occurs when using a staggered arrangement for the pressure as well as the velocity fields. For that purpose, let us consider the variables distribution as depicted in Figure 4. In the one-dimensional case, we may observe that the interface I is always taken on nodes. Therefore, the first derivatives in (13) are computed by second-order space-decentered scheme based on Taylor series expansion with points distribution illustrated for variables on nodes and centers in Figure 4.

It is well known that the Poisson-Neumann problem is singular (see Pozrikidis (2001)). Within a multidomains framework, this singularity occurs in the resolution of the interface through the linear system (14). To overcome this difficulty a Tikhonov regularization is used through a singular value decomposition (SVD) of \mathcal{M} associated with the pressure. Such an operation is performed in a preprocessing stage. The resolution of (3) in a subdomain is thus obtained through two steps at each iteration. First, the problem \mathcal{P}_1 is computed. The second member \mathcal{H} of (14) is thus evaluated. The interface values is obtained through the Tikhonov regularized solution

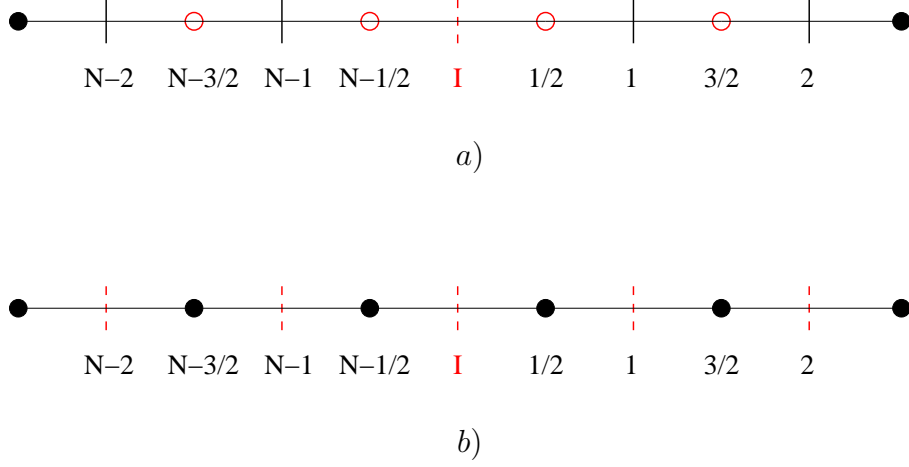


Figure 4: The centers and nodes grid distribution used for the evaluation of the first derivatives at the interface are depicted. The interface is denoted by I . The points taken into account for the evaluation of the first derivative are represented in red: a) interface associated with fields defined on centers: points considered are displayed in empty circles; b) interface associated with fields defined on nodes: points considered are displayed in dashed lines.

of Σ . Then, the problem (15) is solved.

$$\begin{cases} \Delta \tilde{\phi}_i = S|_{\Omega_i} \text{ in } \Omega_i \\ \tilde{\phi}_i = \phi_i|_{\chi_i} \text{ on } \chi_i \\ \tilde{\phi}_i = \lambda \text{ on } \Upsilon_i \end{cases} \quad (15)$$

with λ the interface values of ϕ_i on Υ_i . Interfaces regarding Helmholtz problems are obtained by means of a LU decomposition of \mathcal{M} with respect to velocity fields. As before, the operation is carried out in a preprocessing stage. Finally, a connectivity table is designed to ensure communication between each subdomain.

3. Global linear stability: theory and numerical method

3.1. Generalities

Within a global linear stability framework, the main hypothesis is that the occurrence of large scale unsteadiness can be described by a bifurcation

theory based on the linearization of the Navier-Stokes operator about an equilibrium state. A recent review of such a method is given by Sipp et al. (2010). Here, we recall the equations governing the space-time nonlinear dynamics of the flow as follows:

$$\frac{\partial \mathbf{u}}{\partial t} = \mathcal{F}(\mathbf{u}) \quad (16)$$

where $\mathbf{u} = {}^t(u, v, w)$ is projected into a free-divergence space and \mathcal{F} the Navier-Stokes operator. A two-dimensional equilibrium state of (16) is referenced hereafter as $\mathbf{U}(x, y)$ with $\mathcal{F}(\mathbf{U}(x, y)) = 0$. The stability of such a solution is governed by the dynamical system (17).

$$\begin{cases} \frac{\partial \tilde{\mathbf{u}}}{\partial t}(\mathbf{x}, t) = \mathcal{A}(\tilde{\mathbf{u}}(\mathbf{x}, t)) \\ \tilde{\mathbf{u}}(x, y, z, t = 0) = \tilde{\mathbf{u}}_0 \end{cases} \quad (17)$$

where $\mathbf{x} = (x, y, z)$, $\tilde{\mathbf{u}}$ is a small perturbation superimposed on \mathbf{U} and \mathcal{A} the Jacobian operator of \mathcal{F} about $\mathbf{U}(x, y)$: $\mathcal{A} = \partial \mathcal{F} / \partial \mathbf{U}$. Solutions of (17) may be thought in the following form:

$$\tilde{\mathbf{u}}(\mathbf{x}, t) = e^{-i\Omega t} \hat{\mathbf{u}}(\mathbf{x}) \quad (18)$$

The asymptotic stability of the system (17) is thus determined by resolving the spectrum of the operator \mathcal{A} . In particular, if $\Omega_i > 0$, the solution $\mathcal{F}(\mathbf{U}(x, y)) = 0$ is asymptotically unstable, whose unsteadiness is characterized by the frequency $\Omega_r/2\pi$ and its spatial structure by $\hat{\mathbf{u}}(\mathbf{x})$.

3.2. Stability equations: 3D periodic perturbations of homogeneous fields in the spanwise direction

As the base flow is homogeneous in the spanwise direction z , we can decompose general perturbations into Fourier modes. Within a linearized framework, modes with different spanwise wave numbers $|\beta|$ are decoupled. As emphasized in Barkley et al. (2002), three-dimensional perturbations can be sought in the following form:

$$\begin{cases} \hat{\mathbf{u}} = (\hat{u}(x, y) \cos \beta z, \hat{v}(x, y) \cos \beta z, \hat{w}(x, y) \sin \beta z) \\ \hat{p} = \hat{p}(x, y) \cos \beta z \end{cases} \quad (19)$$

In order to use a linearized version of the DNS code described in previous section, the system (17) may be rewritten in a flux conservative formulation as:

$$\left\{ \begin{array}{l} \frac{\partial \hat{u}}{\partial t} + 2 \frac{\partial U \hat{u}}{\partial x} + \frac{\partial U \hat{v}}{\partial y} + \frac{\partial V \hat{u}}{\partial y} + U \beta \hat{w} + \frac{\partial \hat{p}}{\partial x} = \frac{1}{Re} \nabla^2 \hat{u} \\ \frac{\partial \hat{v}}{\partial t} + 2 \frac{\partial V \hat{v}}{\partial y} + \frac{\partial U \hat{v}}{\partial x} + \frac{\partial V \hat{u}}{\partial x} + V \beta \hat{w} + \frac{\partial \hat{p}}{\partial y} = \frac{1}{Re} \nabla^2 \hat{v} \\ \frac{\partial \hat{u}}{\partial t} + \frac{\partial U \hat{w}}{\partial x} + \frac{\partial V \hat{w}}{\partial y} - \beta \hat{p} = \frac{1}{Re} \nabla^2 \hat{w} \\ \frac{\partial \hat{u}}{\partial x} + \frac{\partial \hat{v}}{\partial y} + \beta \hat{w} = 0 \end{array} \right. \quad (20)$$

This formulation is then well adapted to the Mac staggered grid depicted in Figure 1. The two-dimensional case is straightforward by considering $\beta = 0$.

3.3. Equilibrium state

A large variety of methods are exposed by several authors to determine the equilibrium state $\mathcal{F}(\mathbf{U}(x, y)) = 0$ of (16). Among these, one may argue that imposing the symmetry of the system (16) is the most obvious solution. Starting from an initial guess, a Newton procedure may also be used to achieve this (see Tuckerman and Barkley (2000) and Knoll and Keyes (2004) for a recent review). Otherwise, both approaches can not be apparent or involve several computational efforts. An easy way to deal with the stationary state is to consider a temporal filtering technique. This method was firstly employed in a global modes framework by Åkervik et al. (2006). The equations (16) are recast as:

$$\left\{ \begin{array}{l} \frac{\partial \mathbf{U}}{\partial t} = \mathcal{F}(\mathbf{U}) - \chi(\mathbf{U} - \mathbf{U}_f) \\ \frac{\partial \mathbf{U}_f}{\partial t} = \frac{\mathbf{U} - \mathbf{U}_f}{\Delta} \end{array} \right. \quad (21)$$

where \mathbf{U}_f denotes the filtered velocity field. The filter cut-off frequency is taken as $f_c = f/2$ with f the frequency of the unsteadiness. A differential form of such a causal-low pass temporal filter combined with a control technique allows to converge until a steady state solution which verifies $\mathcal{F}(\mathbf{U}) = 0$

(21). Δ and χ are the filter width and the amplitude of the control respectively. By following Åkervik et al. (2006), χ has to verify: $\Omega_i < \chi < \Omega_i + 1/\Delta$ where Ω_i is associated with the least damped eigenvalue. In the next part, both the symmetry method and the filtering technique are applied. Regarding the last method, the system (21) is solved by marching forward in time both the term $\chi(\mathbf{U} - \mathbf{U}_f)$ and the filtering field with an AB3. A residual criterion is based on $r_{bf} = \max_{\mathcal{D}} |\mathbf{U} - \mathbf{U}_f|$ as in Åkervik et al. (2006).

3.4. Matrix-free framework: a multidomains strategy

Within a matrix-free framework, the dominant eigenmodes of \mathcal{A} are approximated by generating a Krylov subspace of dimension N based on several snapshots of the system (17) which is initiated by a perturbation $\tilde{\mathbf{u}}_0$. Such a method is well detailed by Saad (2003) and is applied with success in several single domain configurations in both three- (Tezuka and Kojiro (2006), Bagheri et al. (2009b) and Feldman and Gelfat (2010)) and two-dimensional geometries (Barkley and Blackburn (2008), Bagheri et al. (2009a) and Bres and Colonius (2008)). We will briefly introduce the notations and numerical methods within a single domain framework. The action of the operator (17) upon an initial perturbation during an evolution time interval ΔT is

$$\tilde{\mathbf{u}}(t = \Delta T) = \mathcal{B}(\Delta T) \tilde{\mathbf{u}}_0, \text{ where } \mathcal{B}(\Delta T) \text{ is formally } e^{\mathcal{A}\Delta T} \quad (22)$$

One may precise that such an operation is achieved through the system (20). A sequence of N snapshots of (17) may thus be expressed as:

$$\mathcal{S}_N = \left(\tilde{\mathbf{u}}_0, \mathcal{B}(\Delta T) \tilde{\mathbf{u}}_0, \mathcal{B}(\Delta T)^2 \tilde{\mathbf{u}}_0, \dots, \mathcal{B}(\Delta T)^{N-1} \tilde{\mathbf{u}}_0 \right) = (S_1, \dots, S_N) \quad (23)$$

An Arnoldi algorithm based on a Gram-Schmidt orthonormalization of the sequence (23), denoted by ${}^\perp\mathcal{S}_N = ({}^\perp S_1, \dots, {}^\perp S_N)$, leads to the following system:

$$\mathcal{B}(\Delta T) {}^\perp\mathcal{S}_N = {}^\perp\mathcal{S}_N \mathcal{H} + r^t \mathbf{e}^\perp S_{N+1} \quad (24)$$

with r a residual, ${}^t\mathbf{e} = (0, 0, 0, \dots, 0, 1)$ a canonical vector of dimension N . \mathcal{H} is an upper Hessenberg matrix of dimension $N \times N$. Therefore, the dominant eigenmodes of $\mathcal{B}(\Delta T)$ are approximated through the eigenmodes of the reduced matrix \mathcal{H} . Let us now adapt such an algorithm to our multidomains strategy. At first, we may point out that global unsteadiness is felt all over the flow fields. Hence, this feature allows in processing with subdomains, by forming sequences which contain only data from each block of the full

domain. This idea is recently suggested by Schmid (2010). Nevertheless, the author has not applied this strategy in a multidomains framework. For that purpose, it is convenient to use the connectivity table realized in the DNS code which links all subdomains to eachothers. Subdomains are denoted by \bullet^p . The algorithm is detailed in **Algorithms** a). The inner product \langle, \rangle is based on the kinetic energy. An in-house code is employed to achieve such an algorithm. Next, the matrix-free method underlying subsets of the full domain will be validated by **Algorithms** b).

N_b : number of subdomains
 N : number of snapshots
 k : eigenmode

for ($p = 1, N_b$)
 $\mathcal{S}_N^p = (S_1^p, \dots, S_N^p)$:
sequence of snapshots in \mathcal{D}_i .
endfor

for ($p = 1, N_b$)
call **arnoldi**($\mathcal{S}_N^p, N, \Omega_{ik}^p, \Omega_{rk}^p, \hat{\mathbf{u}}_k^p$)
endfor

Calculate $\hat{\mathbf{u}}_k$ in $\mathcal{D}_1 \cup \mathcal{D}_2 \dots \cup \mathcal{D}_{N_b}$ by
means of the connectivity table

a) Each subdomain \mathcal{D}_i is considered.

N_b : number of subdomains
 N : number of snapshots
 k : eigenmode

for ($p = 1, N_b$)
 $\mathcal{S}_N^p = (S_1^p, \dots, S_N^p)$:
sequence of snapshots in \mathcal{D}_i .
endfor

 $\mathcal{S}_N = \mathcal{S}_N^1 \cup \mathcal{S}_N^2 \dots \cup \mathcal{S}_N^{N_b}$
call **arnoldi**($\mathcal{S}_N, N, \Omega_{ik}, \Omega_{rk}, \hat{\mathbf{u}}_k$)

b) The full domain \mathcal{D} is considered.

while (test=0)
Orthonormalize \mathcal{S}_N : $^\perp \mathcal{S}_N$, by a modified Gram-Schmidt algorithm
if ($(\max_{i,j} <^\perp S_i, ^\perp S_j >) < 10^{-16}$)
for $i \neq j$ with $(i, j) \in (1, \dots, N)^2$
test=1
endif
endwhile

for ($i = 1, N$)
 $\mathcal{B}(\Delta T) \ ^\perp S_i = \mathcal{B}(\Delta T)(S_i) -$
 $\sum_{k=1}^{i-1} \frac{<^\perp S_k, S_i >}{<^\perp S_k, ^\perp S_k >} \mathcal{B}^p(\Delta T) (^\perp S_k)$
with $\mathcal{B}(\Delta T)(S_i) = (S_{i+1})$
endfor

- Calculate \mathbf{H} ,
 $H_{i,j} = <\mathcal{B}(\Delta T)^\perp S_i, ^\perp S_j >$
- Calculate eigenvalues d_k and eigenvectors $\hat{\mathbf{u}}_k$ of \mathbf{H} with the QR routine ZGEEV from LAPACK library
- Calculate eigenvalues of $\mathcal{B}(\Delta T)$:
 $(\Omega_i)_k = \Re(\ln(d_k) / \Delta T)$
 $(\Omega_r)_k = \Im(\ln(d_k) / \Delta T)$
- Eigenvectors of $\mathcal{B}(\Delta T)$: $\hat{\mathbf{u}}_k$

c) **arnoldi**($\mathcal{S}_N, N, \Omega_{ik}, \Omega_{rk}, \hat{\mathbf{u}}_k$)

Algorithms: Time-stepping strategy based on the full domain \mathcal{D} and subsets of \mathcal{D} .

4. Lid-driven cavity flow at $Re = 900$

In the present part, the ability as well as the accuracy of the global stability matrix-free method are assessed by computing dominant eigenmodes. The benchmark lid-driven cavity at $Re = 900$ subjected to three-dimensional per-

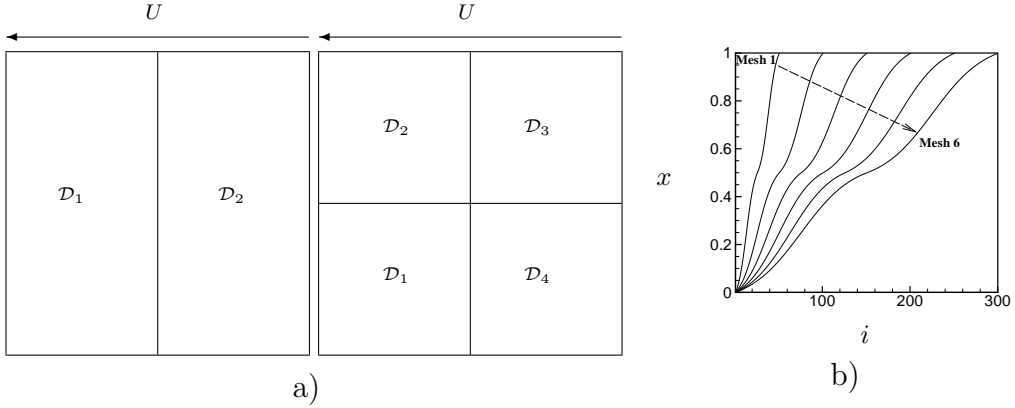


Figure 5: a) Partitions \mathcal{P}_2 , \mathcal{P}_4 considered for the lid-driven cavity flow. \mathcal{P}_1 is obvious. b) The grid points distribution i along the x or y direction is displayed for each mesh associated with the lid-driven cavity flow.

turbation is investigated. The critical Reynolds number associated with the emergence of three-dimensional structures is given by Theofilis et al. (2004): $Re = 782.61$. In the first section, the base flow is computed by restricting the computational domain to a $2D$ flow and by using a time-marching procedure until reaching a residual value based on the infinity norm equals to 10^{-16} .

4.1. Base flow

Three partitions are considered: \mathcal{P}_1 , \mathcal{P}_2 and \mathcal{P}_4 , composed of 1 domain, 2 subdomains and 4 subdomains respectively. \mathcal{P}_2 , \mathcal{P}_4 are displayed in Figure 5 a). 6 irregular meshes refined near interfaces and boundaries are generated from (50×50) to (300×300) . In all cases, the same meshes are used for \mathcal{P}_1 , \mathcal{P}_2 and \mathcal{P}_4 . The grid points distribution for both of them is illustrated in Figure 5b). The finest irregular grid (300×300) is taken as a reference. One may observe in Figures 6 that all partitions match very well. In particular, continuity properties through the interfaces are correctly treated for both pressure and velocity fields.

4.2. Three-dimensional periodic global modes at $Re = 900$

The benchmark problem considered in this section is the periodic case in the spanwise direction analyzed by Theofilis et al. (2004) at $Re = 900$ with the spanwise wavenumber β equals to 7.35. Both the spectrum and the

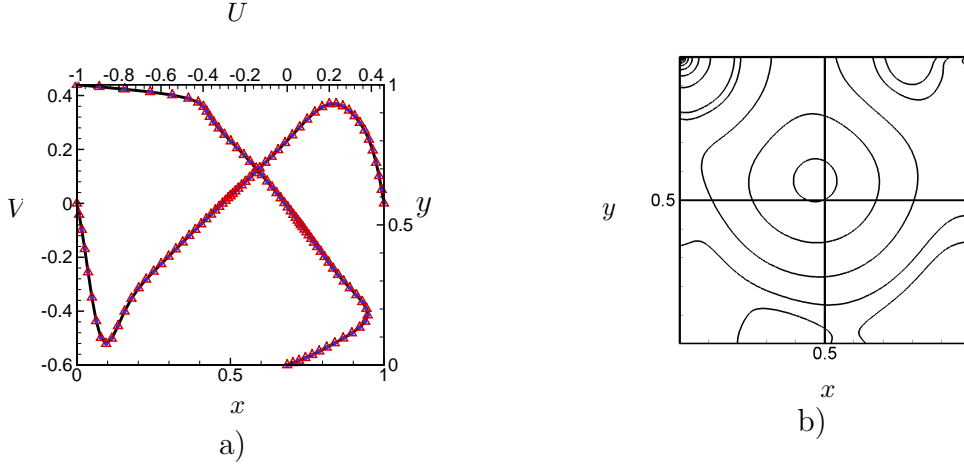


Figure 6: a) The velocity profiles in the lid-driven cavity are plotted at the mid-height and mid-length for $Re = 900$. The mesh (300×300) is considered. \mathcal{P}_1 is displayed in full lines. \mathcal{P}_2 , and \mathcal{P}_4 are plotted with triangles and circles respectively. According to the latter, every 5 points are represented. b) The pressure fields regarding the lid-driven cavity flow at $Re = 900$ is shown in full lines. The partitions \mathcal{P}_1 , \mathcal{P}_2 and \mathcal{P}_4 are considered .

numerical values with respect to the least damped eigenmodes obtained by Theofilis et al. (2004) are displayed in Figure 7 and in Table 1.

4.2.1. Time-stepping: validation of numerical parameters

To examine the validity of time-stepping numerical parameters, we investigate the influence of both the sampling period ΔT and the dimension of the Krylov subspace N on the modes T_1 , T_2 , T_3 and S_1 . The algorithm detailed in **Algorithms** b) is employed. For demonstration purposes, we consider partition \mathcal{P}_1 and the mesh (300×300). ΔT is taken to verify the Nyquist criterion (see Bagheri et al. (2009a)). In this context, we focus on the highest frequency mode, corresponding to T_2 . The linear stability analysis with respect to mode T_2 is conducted by setting $\Delta T = T_{T_2}/32$, where T_{T_2} is the period associated with the mode T_2 , which is 16 times the Nyquist cutoff. A large Krylov subspace of dimension $N = 600$ is taken as a reference value, noted hereafter as \bullet_{ref} . To illustrate the accuracy of the Krylov dimension subspace N , an error criterion is defined by

$$e_r(\Omega_r) = \left| \frac{\Omega_r - (\Omega_r)_{ref}}{(\Omega_r)_{ref}} \right|, \quad e_r(\Omega_i) = \left| \frac{\Omega_i - (\Omega_i)_{ref}}{(\Omega_i)_{ref}} \right| \quad (25)$$

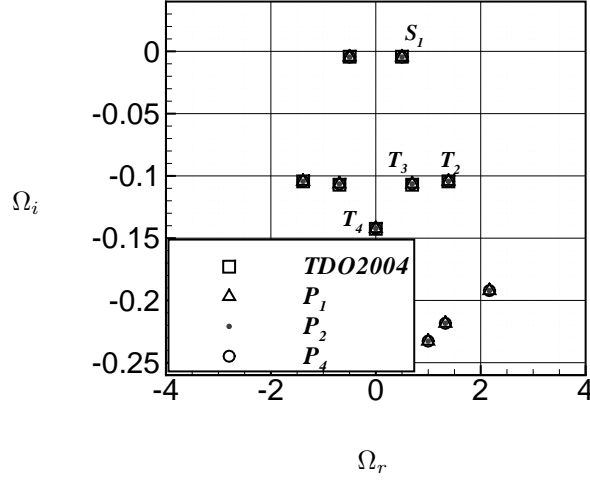


Figure 7: The spectrum of the lid-driven cavity flow subjected to three-dimensional perturbation is shown for $Re = 900$ and $\beta = 7.35$. Values given by Theofilis et al. (2004) are referenced by TDO. The mesh is fixed to (300×300) . \mathcal{P}_1 , \mathcal{P}_2 and \mathcal{P}_4 are considered in our computations.

Mode	Ω_r (TDO)	Ω_i (TDO)	Ω_r	Ω_i
T_1	± 0.4981	-0.0043	± 0.4997	-0.0046
T_2	± 1.3846	-0.1044	± 1.3867	-0.1044
T_3	± 0.6928	-0.1071	± 0.6934	-0.1064
S_1	0.0000	-0.1425	0.0000	-0.1423

Table 1: The complex circular frequencies obtained by Theofilis et al. (2004) (referenced as TDO) with regards to modes T_1 , T_2 , T_3 and S_1 . Values are compared with those computed in this manuscript by considering the full domain \mathcal{D} (algorithm **Algorithms** b) and mesh (300×300) . Results are independent of partitions \mathcal{P}_1 , \mathcal{P}_2 and \mathcal{P}_4 considered at numbers of significant digits given.

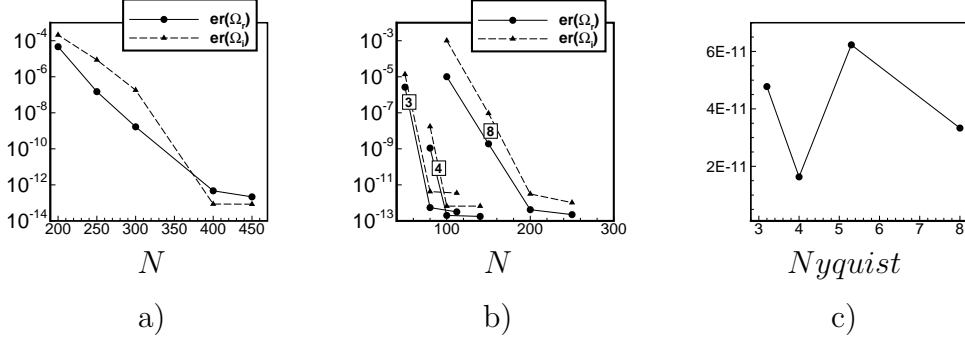


Figure 8: a), b) Mode T_2 is considered. c) Mode S_1 is considered. N is the Krylov dimension subspace. a) $-\log_{10}(er(\Omega_r/i))$ is plotted with respect to $\Delta T = T_{T_2}/32$ where T_{T_2} is the period of mode T_2 . b), c) $-\log_{10}(er(\Omega_r/i))$ is plotted with respect to $\Delta T = T_{T_2}/8$, $\Delta T = T_{T_2}/4$ and $\Delta T = T_{T_2}/3$.

As shown in Figure 8 a), we may observe a convergence of e_r with an accuracy $\approx 10^{-13}$ until to reach a saturated value for both Ω_r and Ω_i . Let us now investigate the influence of ΔT . For that purpose, three sampling frequencies are chosen, corresponding to 8, 4 and 3 times the Nyquist criterion respectively. The values of e_r are depicted in Figure 8 b) by increasing the Krylov subspace N . One may observe that up to sampling frequency of about three times the Nyquist cutoff, the residual error is less than 10^{-11} . In particular, a Krylov subspace of dimension $N = 100$, which corresponds to approximately 15 periods, is sufficient to observe a saturation of the Arnoldi algorithm regarding the largest sampling time. Therefore, this analysis suggests that a sampling frequency superior to 3 times the Nyquist cutoff and a total sampling time larger than 15 periods are appropriate. As a consequence, the least damped unstationnary eigenmodes T_1 , T_2 and T_3 are computed by setting $\Delta T \approx 0.75$ equals to three times the Nyquist cutoff underlying mode T_2 , and a Krylov subspace of dimension $N = 300$. Hence, both modes T_1 and T_3 verify the criterion defined above. Such criterion may not be defined for the stationnary mode S_1 . Now, we study the influence of ΔT based on the Nyquist criterion associated with T_2 . As above, the reference value is taken for a frequency sampling equals to 16 times the Nyquist cutoff and $N = 600$. It may be observed in Figure 8 c) that the residual error is less than 10^{-11} by varying the sampling frequency. It implies that the time-stepping numerical parameters defined above ensure a sufficient accuracy to calculate T_1 , T_2 , T_3

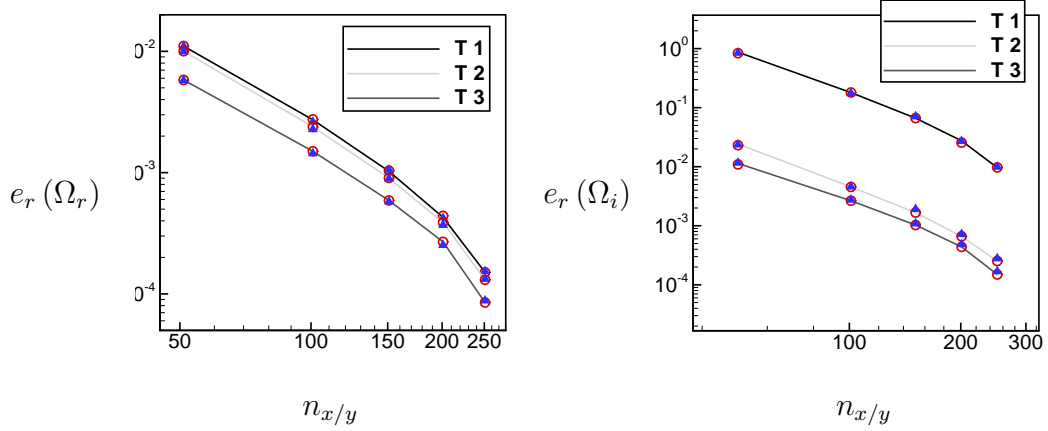


Figure 9: Maximum relative error of the global circular frequency associated with M_1 , M_2 and M_3 as function of the mesh refinement: $n_{x/y}$ (number of grid points according to $x/$ or y) for Mesh 1 \rightarrow 5 (see figure 5b). Results with respect to \mathcal{P}_1 , \mathcal{P}_2 and \mathcal{P}_4 are displayed in full lines, triangles and circles respectively.

and S_1 . For these parameters, the temporal amplification rates and circular frequencies with regards to T_1 , T_2 , T_3 and S_1 are referenced in Table 1 and displayed in Figure 7. In addition, a good agreement is observed compared to the data from Theofilis et al. (2004).

4.2.2. Influence of the domain decomposition

Several simulations are then carried out with different meshes as displayed in Figures 5 b). The reference values are associated with \mathcal{P}_1 and a mesh (300×300) . In order to measure the effect of the partitioning on the modes T_1 , T_2 , T_3 , we also consider \mathcal{P}_2 and \mathcal{P}_4 . The stability calculations are carried out by considering the full domain \mathcal{D} (algorithm **Algorithms** b)). $e_r(\Omega_{r/i})$ are plotted in Figure 9 for each partition and T_1 , T_2 and T_3 . One may observe that the convergence rate is not affected by the partitioning. In particular, both temporal amplification rate and circular frequency converge to the same value $\Omega_{r/i}(ref)$ associated with \mathcal{P}_1 . The eigenvalues are also reported in Figure 7.

In the end, perturbation velocity fields with respect to T_1 are plotted in Figure 10 regarding the finest grid mesh. Once again, it shows that continuity properties through interfaces are well solved.

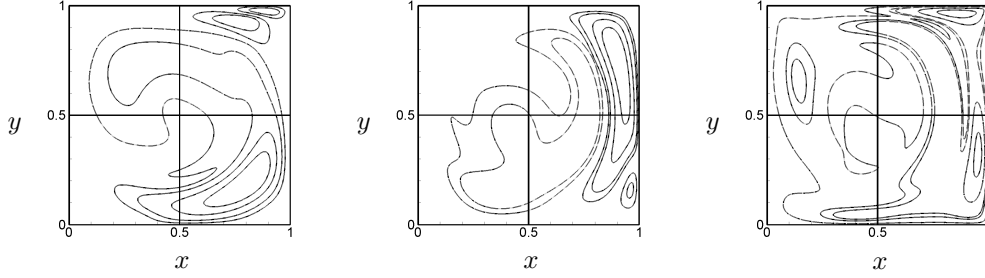


Figure 10: Perturbation velocity fields associated with T_1 is shown. The mesh is fixed to (300×300) . \mathcal{P}_1 , \mathcal{P}_2 and \mathcal{P}_4 are considered in full, dashed and dotted lines respectively. The streamwise, normal and spanwise components are ordered from the left to the right.

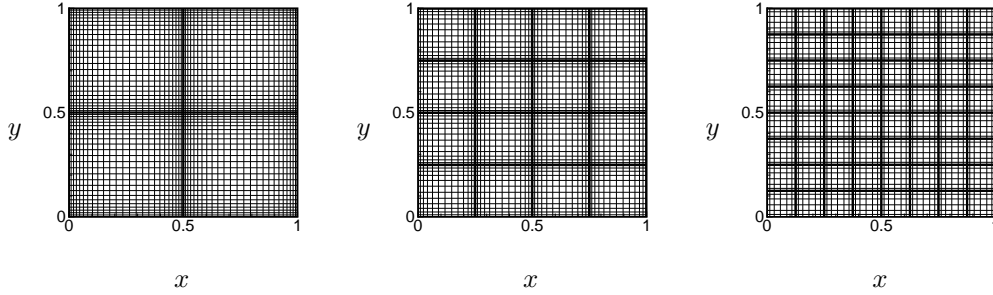


Figure 11: Partitions referenced as \mathcal{P}_4 , \mathcal{P}_{16} and \mathcal{P}_{64} are illustrated. Every six meshes are plotted in each direction.

4.2.3. Efficiency of the algorithm

Let us now investigate the possibility of parallel computations with respect to our multidomains matrix-free method. For that purpose, 3 partitions are considered denoted as \mathcal{P}_4 , \mathcal{P}_{16} and \mathcal{P}_{64} composed by 4, 16 and 64 subdomains respectively. The mesh grid is set to (300×300) and are shown in Figure 11. The number of grid points in both directions x and y is equal in each subdomain. The snapshots are performed in each subdomain with respect to \mathcal{P}_4 , \mathcal{P}_{16} and \mathcal{P}_{64} . The Arnoldi algorithm **Algorithms a)** is then applied to recover eigenmodes in the entire geometry. The mode T_2 is taken into account to illustrate our purpose. Error values defined in (25) for each subdomain are then computed. The reference value is defined in the previous section. In Figure 12, we plot in a logarithmic scale, the different values of $e_r(\Omega_r)$ and $e_r(\Omega_i)$. The error is about 10^{-4} according to Ω_i and 10^{-5} with

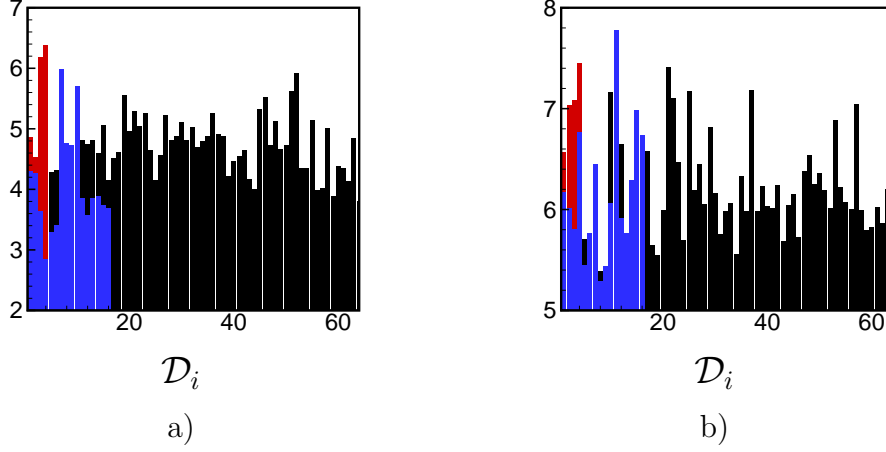


Figure 12: $-\log_{10}(er)$ with respect to Ω_i a) and Ω_r b) are plotted for each subdomain according to \mathcal{P}_4 (in red), \mathcal{P}_{16} (in blue) and \mathcal{P}_{64} (in black).

respect to Ω_r which is less than the accuracy obtained from the full domain \mathcal{D} as depicted in Figure 9. Similar behaviour is observed according to T_1 , T_3 and S_1 . Also, it may be underlined the possibility of recovering the eigenfunction from those associated with each subdomain \mathcal{D}_i . In this context, the mode T_1 is rebuilt as described in **Algorithms a)**. The eigenfunction is well recovered for \mathcal{P}_4 , \mathcal{P}_{16} and \mathcal{P}_{64} as shown in Figure 13. In particular, the continuity between each subdomain is well satisfied whereas it is not imposed directly. As a consequence, our multidomains strategy seems to be a natural way to exploit parallel architectures. To illustrate our purpose, we defined a speed-up as $S_p = t_{md}/t_{sd}$ where t_{md} corresponds to the CPU time regarding the partition \mathcal{P}_i ($i = 1, 4, 16$ or 64) and t_{sd} corresponds to the CPU time with respect to one subdomain. S_p associated with the Arnoldi algorithm is shown in Figure 14 a). A linear scaling is observed. A similar procedure is applied to the linearized DNS to generate the sequence of snapshots. We consider thus the CPU time associated with the second stage of Thomas algorithms according to the Helmholtz and Poisson problems employed in the linearized DNS. S_p is plotted in Figure 14 b). It is interesting to remark that Thomas algorithm is more efficient when decreasing the subdomains size. To further illustrate this comment, the dimensionless cpu time according to the total time: $t_{tot} = t_{dtot}/t_{mdtot}$ is plotted in Figure 14 c). t_{dtot} is the total

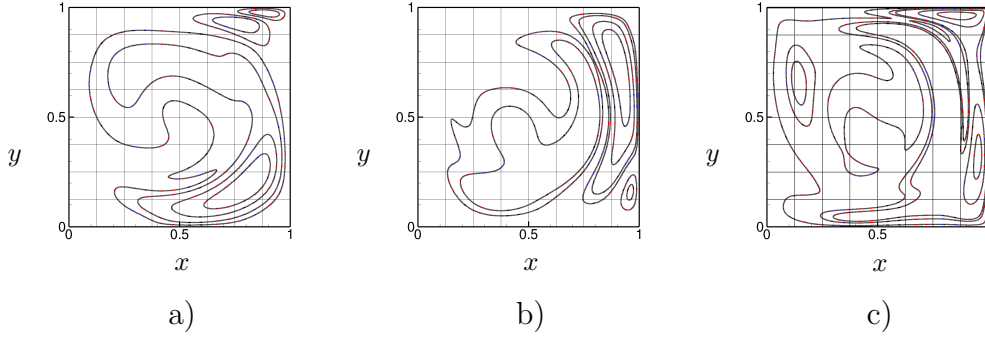


Figure 13: Influence of Arnoldi zonal computations on eigenfunction (**Algorithms a**). a) $|\hat{u}|$, b) $|\hat{v}|$ and c) $|\hat{w}|$. \mathcal{P}_4 , \mathcal{P}_{16} and \mathcal{P}_{64} are superimposed. The mode T_1 is considered.

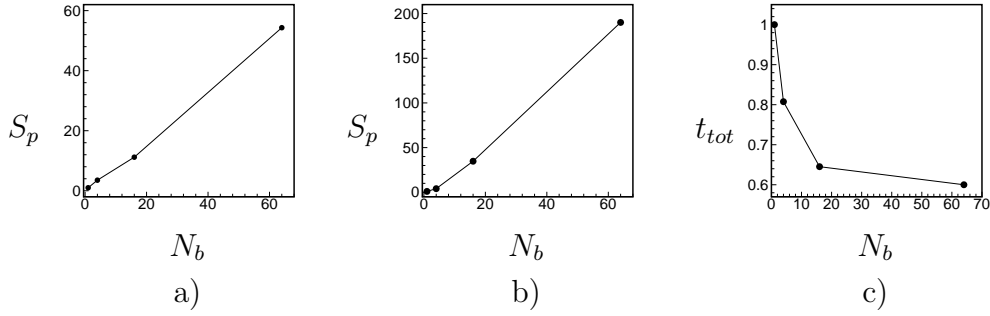


Figure 14: Dimensionless times according to a) the Arnoldi algorithm **Algorithms a**) b) The second stage of the Thomas algorithm c) The total time underlying linearized DNS

time with regards to \mathcal{P}_1 and t_{mdtot} is the total time associated with \mathcal{P}_4 , \mathcal{P}_{16} and \mathcal{P}_{64} . One may remark that the partitioning yields to reduce the total time consuming which is in agreement with S_p . Similar behaviour underlying linear system in a multidomains framework is reported by Raspo (2003).

5. Flow past a square cylinder

To assess the ability of our multidomains method to describe an oscillator behavior underlying open flows, the classical benchmark problem of a 2D flow around a square cylinder is investigated in this section. The selected geometry is similar to the one of Breuer et al. (2000), Abide and Viazzo

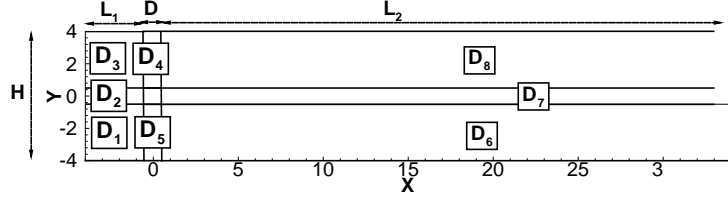


Figure 15: Domain partitioning of the flow past a square cylinder.

(2005) and Camarri and Iollo (2010). It is composed of a square cylinder with a diameter $D = 1$, centered inside a plane channel of height $H = 8$. The geometry as well as the partitioning are illustrated in Figure 15. A parabolic inlet velocity profile is prescribed at the inflow. The system (1) is closed by wall and outflow boundary conditions. The Reynolds number based on maximum inlet velocity u_{max} and square cylinder diameter D is fixed at $Re = 60$, which is slightly above the critical value ≈ 58 (see Camarri and Iollo (2010)).

5.1. Base flow

A critical point concerning open-flows is associated with the placement of domain boundaries. To guarantee a relevant base flow and linear dynamics, stationary computations are carried out on 7 different meshes summed up in Table 2 referenced as \mathcal{C}_i . Each mesh is refined near the walls of the square cylinder and on upper as well as lower wall boundaries. The case \mathcal{C}_3 is illustrated in Figure 16. A Fourier analysis of the unsteady computation (see Figure 16 a)) indicates a Strouhal number $S_t \approx 0.12$, which is equivalent to the value obtain by Breuer et al. (2000). The cutoff frequency and the amplitude of the filter are fixed to $f_c = S_t/2$ and $\chi = 0.2$ respectively. Concerning the latter, χ is determined a posteriori by computing the temporal amplification rate with respect to the dominant eigenmode. The convergence of the equilibrium state for \mathcal{C}_3 and \mathcal{C}_4 are depicted in Figure 17 a) versus time. One may observe that the latter is unaffected by the grid resolution. A residual value $\approx 10^{-12}$ is reached after 70 periods of the vortex shedding cycle. The base flow is illustrated in Figure 16 b). The filtering technique has for consequence to symmetrize the flow which is consistent with the axial symmetry.

Let us investigate the influence of geometry parameters on the convergence toward a steady state. In Figure 17 b), the size of the recirculation length L_r versus L_1 is plotted. It appears that $L_1/D = 10$ is sufficient to reach a converged steady state. One may precise that both influence of the grid

	L_1	L_2	D_1	D_2	D_3	D_4	D_5	D_6	D_7	D_8
\mathcal{C}_1	4	35	181×171	181×81	181×171	81×171	81×171	211×171	211×81	211×171
\mathcal{C}_2	6	40	165×151	165×61	165×151	61×151	61×151	211×151	211×61	211×151
\mathcal{C}_3	6	45	200×171	200×81	200×171	81×171	81×171	231×171	231×81	231×171
\mathcal{C}_4	6	40	210×181	210×91	210×181	101×181	101×181	251×181	251×91	251×181
\mathcal{C}_5	8	45	210×171	210×81	210×171	81×171	81×171	231×171	231×81	231×171
\mathcal{C}_6	10	45	250×171	250×81	250×171	81×171	81×171	231×171	231×81	231×171
\mathcal{C}_7	12	45	260×171	260×81	260×171	81×171	81×171	231×171	231×81	231×171

Table 2: Mesh size in each subdomain ($n_x \times n_y$).

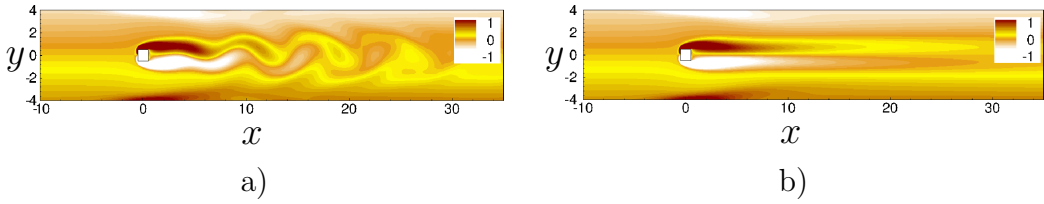


Figure 16: The square cylinder flow at $Re = 60$ is displayed through a) Contour plots of instantaneous vorticity fields. b) Contour plots of the vorticity fields associated with the equilibrium state.

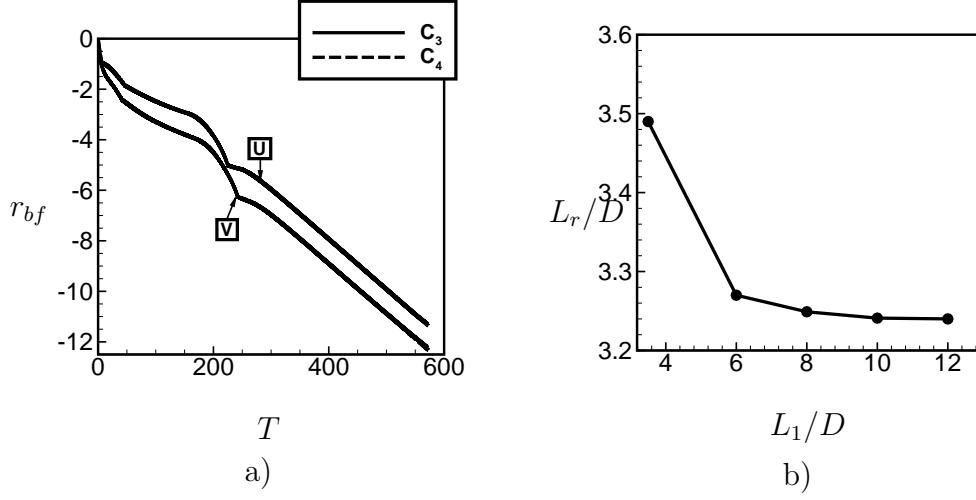


Figure 17: a) Residual value according to an equilibrium state versus dimensionless time. b) Recirculation length of the steady state versus L_1 .

mesh and L_2 with respect to C_3 have proven to not affect the results. A recirculation length $L_r/D = 3.242$ is found consistent with Breuer et al. (2000) formulae $L_r/D = -0.065 + 0.0554 \times Re = 3.259$.

5.2. Two-dimensional unstable global mode

5.2.1. Influence of time-stepping numerical parameters

The case C_3 is considered to evaluate the influence of time-stepping parameters on the unstable global mode. Snapshots in the full domain \mathcal{D} are taken into account. At first, the sampling time between two consecutive snapshots is fixed to $\Delta T = T/32$, with T the unsteadiness period, which is 16 times the Nyquist criterion. In this way, a large Krylov subspace $N = 600$ is used as a reference case. From Figure 18, one may observe that a Krylov subspace dimension ≈ 400 is sufficient to reach a residual $\approx 10^{-12}$ for both the temporal amplification rate and the circular frequency. Hence, ΔT is decreased. The sampling frequencies are fixed to 5 and 3 times the Nyquist criterion. The results are displayed in Figure 18. As a consequence, $\Delta T = T/6$ and $N = 140$ provide the same accuracy as for the reference case. Hence, these parameters are used in all the next computations.

Both grid and L_2 dependencies with respect to subdomains $\mathcal{D}_4 \cup \mathcal{D}_5 \cup \mathcal{D}_6 \cup \mathcal{D}_7 \cup \mathcal{D}_8$ are investigated by considering C_2 , C_3 and C_4 . Results are

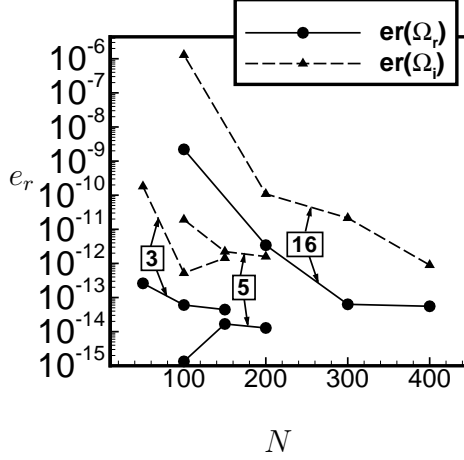


Figure 18: Influence of time-stepping numerical parameters with respect to \mathcal{C}_3 . $3\times$, $5\times$ and $16\times$ Nyquist criterion are considered. The reference case is given for $16\times$ the Nyquist criterion and $N = 600$.

reported in table 3 a). Then, the influence of L_1 is evaluated in agreement with the accuracy given by \mathcal{C}_3 . The table 3 b) establishes that the dominant eigenvalue is unaffected when $L_1/D > 10$. From the above discussion, \mathcal{C}_6 is an appropriate reference case.

5.2.2. Influence of the domain partitionning

To check the influence of the partitioning on the global stability, we consider three partitions with respect to \mathcal{C}_6 , referenced as \mathcal{P}_8 , \mathcal{P}_{11} and \mathcal{P}_{14} , associated with 8, 11 and 14 subdomains, respectively. They are depicted in Figure 19. The reference value is given by the global stability analysis performed on the full domain regarding \mathcal{P}_8 . Then, the Arnoldi algorithm described in **Algorithm a)** is performed in each subdomain according to snapshots of the linearized DNS underlying \mathcal{P}_8 , \mathcal{P}_{11} and \mathcal{P}_{14} . The error e_r is plotted in Figure 20. The analysis emphasizes that the error until 14 subdomains does not exceed 0.1% of the reference value which is less than precision of the scheme according to this discretization. Eigenfunctions are displayed in Figure 21 for each partitioning \mathcal{P}_8 , \mathcal{P}_{11} and \mathcal{P}_{14} . One may underline that the partitioning has no influence on the eigenfunction. In particular, it is also suprising to notice that the global mode is well computed in subdomains \mathcal{D}_1 , \mathcal{D}_2 and \mathcal{D}_3 whereas it concentrates a small part of its spatial support.

	\mathcal{C}_2	\mathcal{C}_3	\mathcal{C}_4
S_t	0.118340975	0.118461761	0.118508091
Ω_i	0.008864661	0.008781478	0.008754140

a)

	\mathcal{C}_3	\mathcal{C}_5	\mathcal{C}_6	\mathcal{C}_7
S_t	0.1185	0.1181	0.1180	0.1180
Ω_i	0.0088	0.0087	0.0087	0.0087

b)

Table 3: a) Analysis of grid dependency on the unstable global mode. b) Analysis of L_1 influence on the unstable eigenmode.

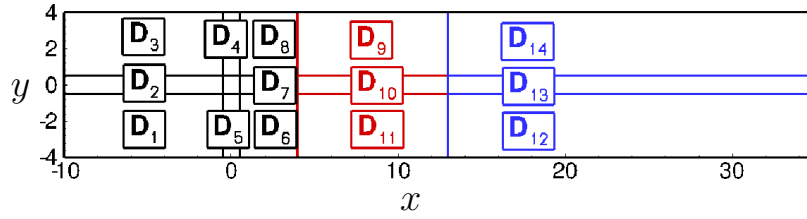


Figure 19: Partitions taken into account in the section 5.2.2: black \mathcal{P}_8 , red \mathcal{P}_{11} and blue \mathcal{P}_{14} .

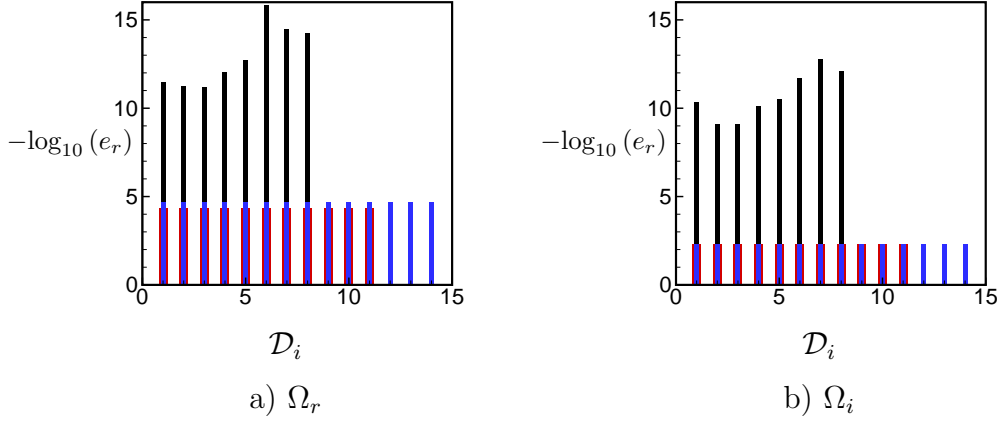


Figure 20: Error e_r analysis in each subdomains with respect to partitioning \mathcal{P}_8 , \mathcal{P}_{11} and \mathcal{P}_{14} (see Figure 19).

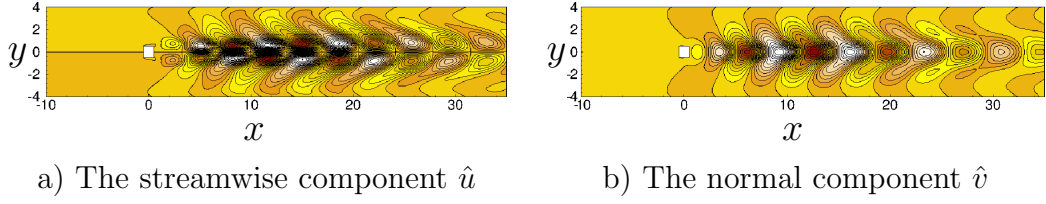


Figure 21: Perturbation velocity fields associated with the square cylinder at $Re = 60$. The linear global stability analysis performed on the full domain regarding \mathcal{P}_8 is displayed in flood. The analysis on subsets according to \mathcal{P}_8 , \mathcal{P}_{11} and \mathcal{P}_{14} are displayed in full lines.

6. Flow past over an open cavity

The main feature of low-Mach-number open cavity flows consists of the generation of vortices at the leading edge of the cavity arising from Kelvin-Helmholtz instability. Their advection along the shear layer yields impingement at the trailing edge and injection of vortical structures inside the cavity. This kind of instability is referred to as shear-layer mode or Rossiter mode. Recently, some aspects of three-dimensional features have been investigated in a compressible regime by Bres and Colonius (2008). They showed that, besides the shear-layer mode, additional three-dimensional lower frequency modes could exist which are mainly localized inside the cavity. From the above discussion, it appears that aside its physical interest, the description of the disturbance behaviour of such a flow is a wonderful numerical benchmark concerning the efficiency of the method to deal with a wide variety of instability phenomena in multi-connected rectangular geometries. This case is designed by the ANR **CORMORED** where the **LIMSI** laboratory and **Dynfluid** are participating (see Basley et al. (2010) and Alizard et al. (2010a)).

We consider the flow over a square cavity at Reynolds number $Re_L = 8140$ based on the cavity length L and free-stream velocity U_∞ . The Reynolds number is built as $Re_L = U_\infty L / \nu$, ν the kinematic viscosity of air: $\nu = 1.5 \times 10^{-5} \text{m}^2 \text{s}^{-1}$, $L = 0.1 \text{m}$ and $U_\infty \approx 1.22 \text{ms}^{-1}$.

Four domains are investigated as depicted in Figure 22. On the left-hand side of the leading edge of the cavity, a Blasius profile is initiated at the inflow. The distance from the leading edge is fixed to $x = 4.9$. On the right-hand side of the trailing edge, an outflow Neumann condition is imposed. The grid points are clustered near interfaces and walls. To dissipate vortical structures at the outflow, a grid stretching is implemented. Two meshes are considered. They are displayed in table 4.

6.1. Base flow at $Re_L = 8140$

The two dimensional dynamics is characterized by self-sustained oscillations with respect to the shear layer above the cavity driving injection of eddies inside. Such a mechanism is illustrated in Figure 23 a). A spectral analysis of a time series sample with regards to the vertical velocity, in the middle of the shear layer at the top of the cavity, is performed. The Strouhal number is defined by $S_t = fL/U_\infty$, with f the characteristic frequency. The fundamental frequency is found to be associated with $S_t \approx 0.89$. Inspired by

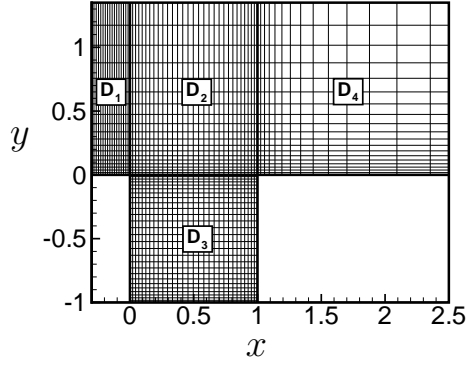


Figure 22: The partition \mathcal{P}_4 associated with the open cavity flows is displayed. Every six meshes are plotted in each direction with respect to mesh 1.

	\mathcal{D}_1	\mathcal{D}_2	\mathcal{D}_3	\mathcal{D}_4
$L_x \times L_y$ (Mesh 1&2)	0.3×2	1×2	1×1	3×2
$N_x \times N_y$ (Mesh 1)	101×131	181×131	181×161	101×131
$N_x \times N_y$ (Mesh 2)	121×151	201×151	201×181	121×151

Table 4: The subdomains characteristics associated with the open cavity flow with respect to Mesh 1 and Mesh 2 are depicted. The subscript $_{x/y}$ refers to the streamwise/normal direction.

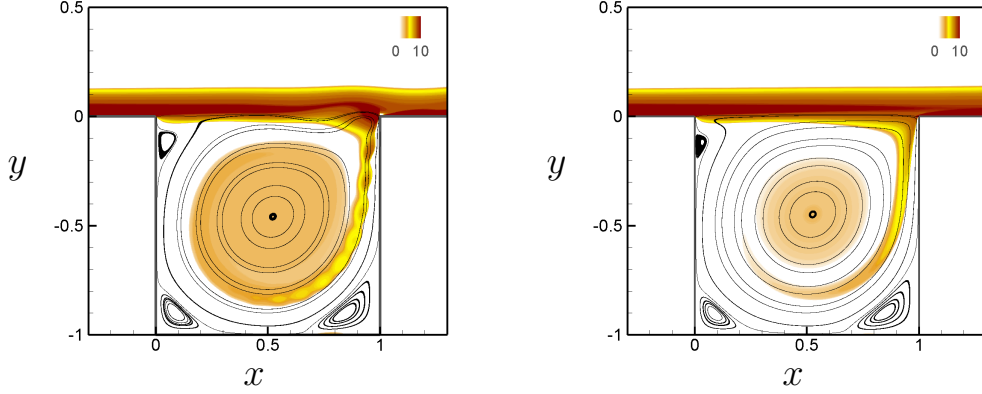


Figure 23: The filtering technique on the open cavity flow at $Re_L = 8140$ is illustrated via a) Contour plots of instantaneous vorticity fields. b) Contour plots of the vorticity fields associated with the equilibrium state. Some streamlines are shown.

the previous analysis, the basic state is given by a filtering technique. For that purpose, the cut-off frequency is given by $f_c = 1/2S_t$ with $S_t = 0.89$. The amplitude of the control is fixed to $\chi = 0.5$. The latter parameter is validated a posteriori. After several time-step iterations, the flow field converges toward a steady state which is displayed in Figure 23 b). One may observe that the shear layer on the top of the cavity relaxes to a steady state. Furthermore, a large recirculating eddy within the cavity is identified. Aside this main feature, three smaller eddies are present near corners on the bottom of the cavity and close to the leading edge corner. These main characteristics are similar to those observed in a square lid-driven cavity flow.

6.2. Two-dimensional global modes

From previous numerical experiments, the sampling frequency is fixed about three-times the Nyquist cutoff. The algorithm depicted in **Algorithms b)** is used. At first, let us investigate a first sequence $S1_N$ regarding a part of the spectrum restricted to $-1.2 < S_t < 1.2$. The time interval between two consecutive snapshots is taken as $\Delta T = 0.14$. The sampling frequency is about three times the Nyquist cutoff. Therefore, the dynamical behaviour with respect to the shear-layer mode is sampled at a sufficiently high frequency. By proceeding as previously, it appears that $N = 100$ snapshots are needed to converge with respect to dominant eigenvalues. The

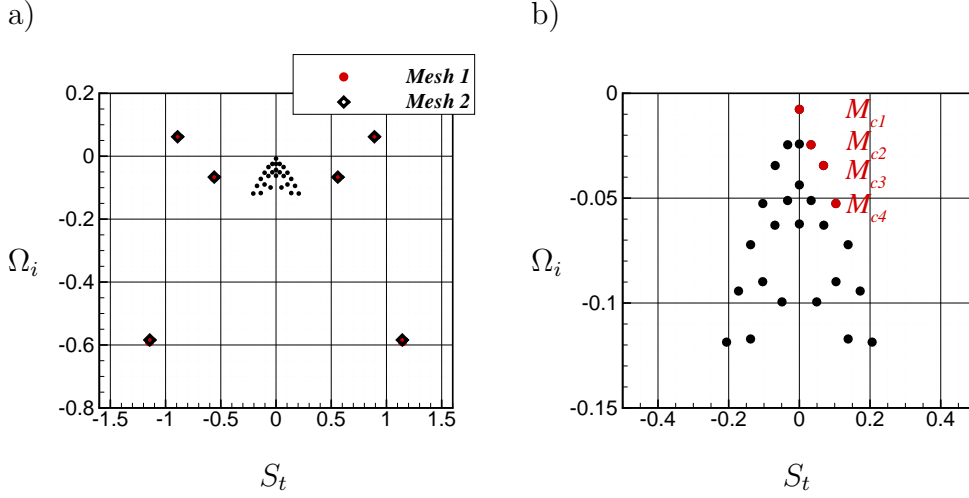


Figure 24: The spectrum according to the 2D dynamics of the flow past an open cavity at $Re_L = 8140$ is shown in a). b) A zoom of the centered part of the spectrum a) is depicted.

extracted spectrum, composed of 6 eigenvalues, is displayed in Figure 24. Only the case $S_t > 0$ is considered, since eigenvalues come in complex conjugate pairs. Ordering modes with regards to their temporal amplification rate, the first, second and third mode oscillate with $S_t^1 = 0.893$, $S_t^2 = 0.560$ and $S_t^3 = 1.146$. Only one unstable mode is identified which is unsteady and whose oscillatory frequency is comparable to the shear-layer mode observed in DNS. The spatial structures of each mode are depicted in Figure 25 using the streamwise and normal velocity components. The energy of the unstable mode has a most significant part inside the shear layer above the cavity. In addition, small-scale features are observed along the shear layer inside the cavity detaching from the trailing edge corner. Overall, it shows good similarities both in terms of spatial wavelength and location with the observed instability in DNS. Global modes with respect to S_t^2 and S_t^3 contain similar characteristics. The convergence property with respect to the grid mesh is now investigated. By considering meshes displayed in Table 4, results appear to differ less than 1% in relative error (see Figure 24).

Aside from this branch, typical spectrum mainly associated with the stable dynamics inside the cavity with lower frequencies are observed in similar configuration by Schmid (2010) and Barbagallo et al. (2009). For that purpose, a second sequence $S2_N$ is considered. A part of the spectrum re-

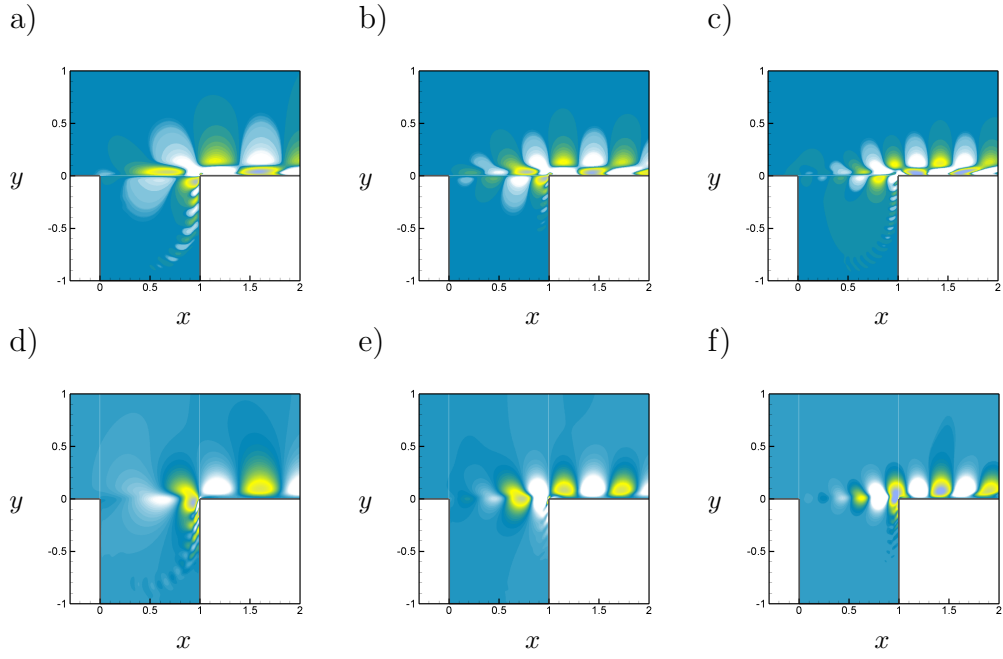


Figure 25: The spatial structures of global modes associated with those displayed in red in Figure 24 a) ordered from the left to the right according to their frequency (S_t^2 , S_t^1 and S_t^3 respectively). The perturbation is visualized by plotting the streamwise component in a), b), c) and the normal component in d), e), f). The unstable mode corresponds to b) and e).

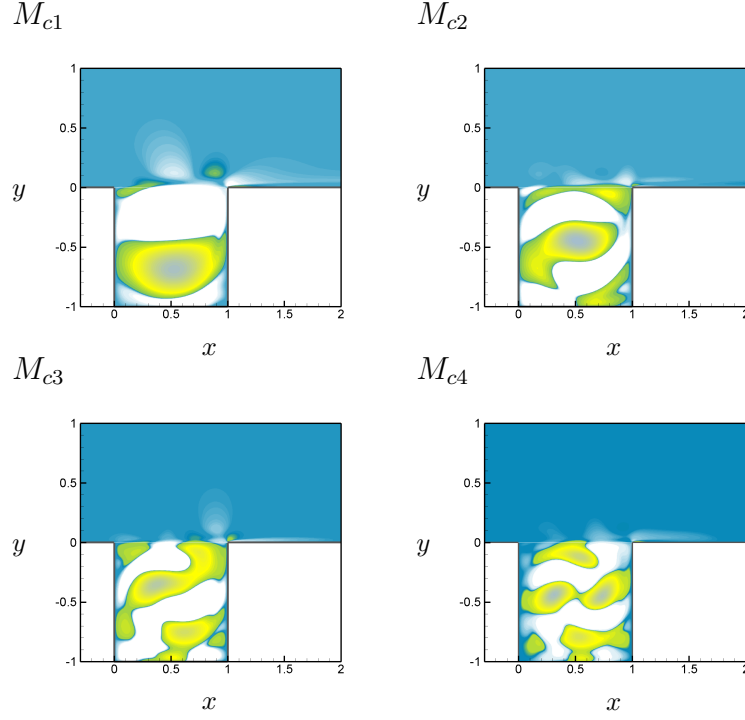


Figure 26: The streamwise velocity components of modes displayed in Figure 24b) are shown.

stricted to $-0.17 < S_t < 0.17$ is explored. Hence, sampling time is fixed to $\Delta T = 0.1$. As in the previous section, experiments on Krylov subspace dimension N show that the convergence requires the use of 200 snapshots. The corresponding spectrum is superimposed on the previous one in Figure 24. A typical parabolic stable branch of lower frequencies is distinguished. The modes referenced as M_{C1} , M_{C2} , M_{C3} and M_{C4} in Figure 24 are illustrated through the streamwise velocity component in Figure 26. One may remark that a major portion is concentrated inside the cavity. These modes are characterized by a cycle of growing and decaying disturbances as it rotates around the main eddy. Furthermore, it shows an increase of more small-scales features inside the cavity with an increase in terms of frequency. Finally, one may recognize a slight influence of the modes along the shear layer above the cavity. Our results are consistent with the observations of Schmid (2010) and Barbagallo et al. (2009). As a consequence, one may be confident about our numerical method to capture this flow dynamics. Then,

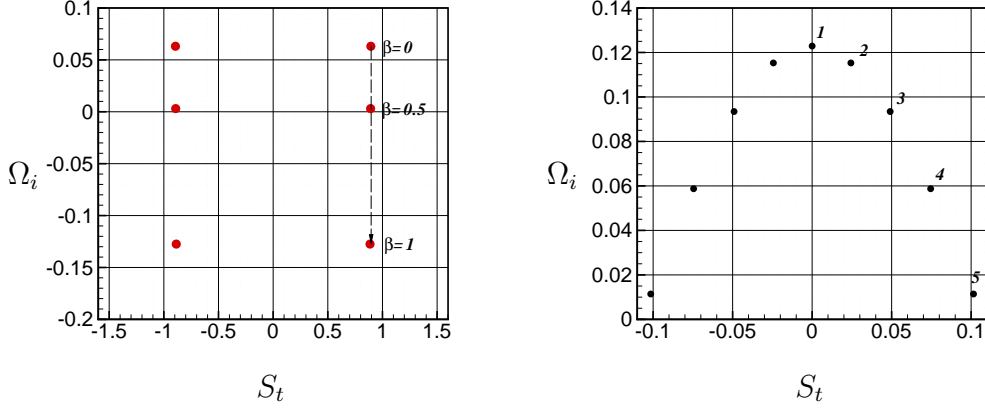


Figure 27: The spectrum with respect to three-dimensional perturbations subjected to the open cavity flow at $Re_L = 8140$ is depicted. On the left: shear-layer mode is displayed by varying β . On the right: global unstable modes are displayed for $\beta = 24$. The ordering used hereafter is referenced via $1 \rightarrow 5$

let us investigate our multidomains strategy and the benefits to use subsets of the full domain subject to three-dimensional periodic perturbation.

6.3. Three-dimensional periodic global modes

The three-dimensional flow past over a rectangular or a square cavity has been investigated recently in an incompressible regime by Chang et al. (2006) using LES and in a compressible regime by Bres and Colonius (2008) using a global linear stability analysis. Both authors reported that the three-dimensional flow instabilities take the form of large-scale spanwise vortices. In particular, Bres and Colonius (2008) identified low-frequency global modes localized inside the cavity as responsible for the low frequency motion observed in several cases (see Chang et al. (2006) and Faure et al. (2009)).

By using the algorithm described in **Algorithm b)**, typical spectra with respect to 3D perturbation are illustrated in Figure 27. The dominant shear-layer mode is clearly damped by an increase of the spanwise wavenumber. In addition to the shear-layer mode, several low-frequency unstable modes emerge with the three-dimensionality. As shown in Figure 28, these modes are mainly concentrated within the cavity. Furthermore, a steady mode is dominant in this configuration with a maximum temporal amplification rate of the same order as the shear-layer mode. These observations are in

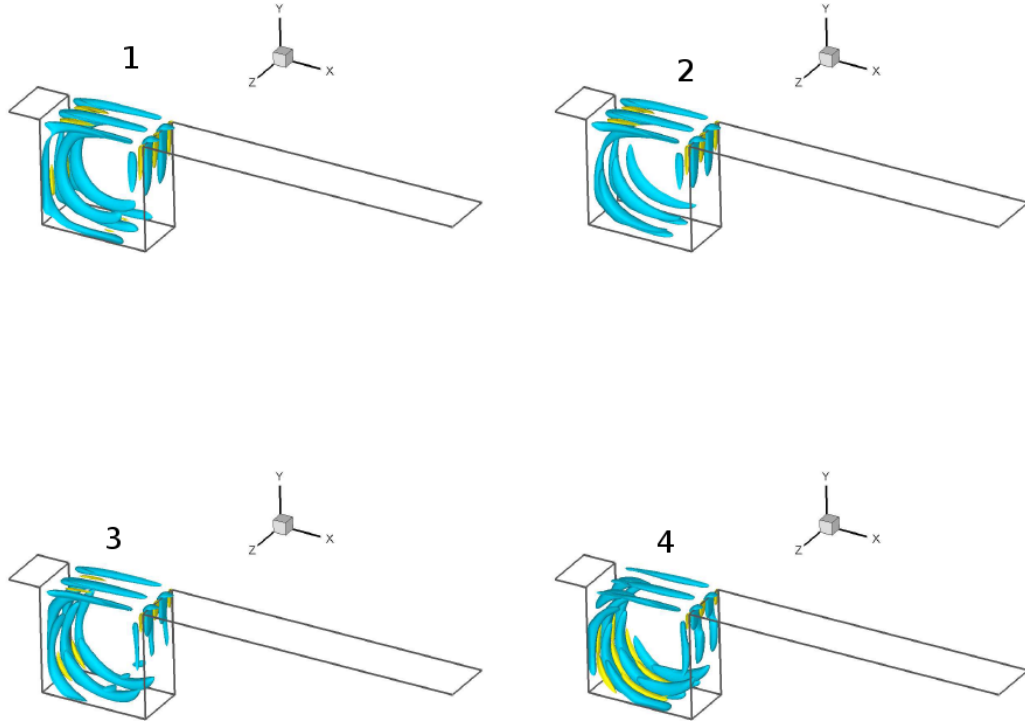


Figure 28: The 3D global mode for $\beta = 24$ with respect to the spectrum in Figure 27 are visualized via their spanwise component of the perturbation. The ordering is similar as in Figure 27.

agreement with the study of Bres and Colonius (2008) in a compressible regime. Within a large range of spanwise wave numbers, its temporal amplification rate depicted in Figure 29 rises to a maximum $\Omega_i = 0.125$ for $\beta = 22$ corresponding to a wavelength $\lambda = 2\pi/\beta \approx 0.3$. This value is in accordance with the one obtained in a compressible regime by Bres and Colonius (2008). Indeed, the authors reported dominant wavelength values equals to $\lambda = 0.5$ and $\lambda = 0.4$ associated with Mach numbers 0.6 and 0.3, respectively, in a similar configuration. In the incompressible limit, our value is closed to the one estimated by Bres and Colonius (2008). The influence of meshes is reported in table 5. One may observe differences on the characteristic variables which do not exceed 0.4%. The influence of domains subdivision on global modes is examined.

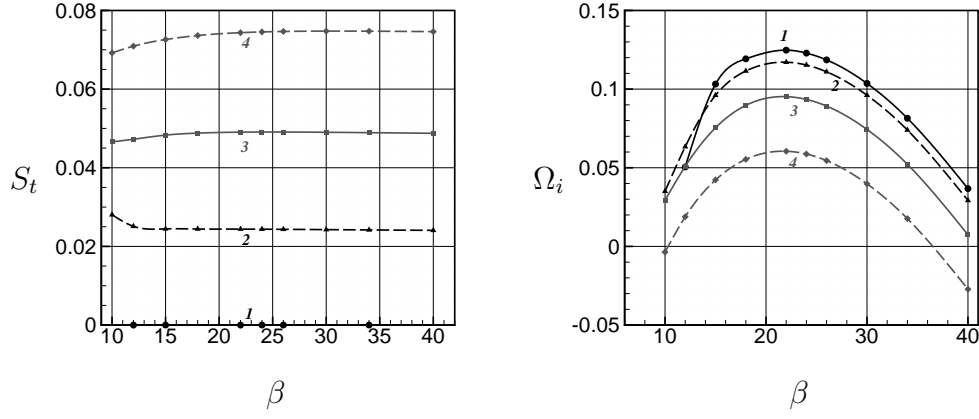


Figure 29: Evolution of frequencies and temporal amplification rates with β according to the dominant three-dimensional global modes.

Mode	S_t (Mesh 1)	Ω_i (Mesh 1)	S_t (Mesh 2)	Ω_i (Mesh 2)
1	0.	0.1228	0.	0.1224
2	0.02438	0.1153	0.02437	0.1148
3	0.04909	0.0934	0.04907	0.0930
4	0.07454	0.0587	0.07451	0.0583

Table 5: Influence of Mesh 1 and Mesh 2 on the spectrum depicted in Figure 27 .

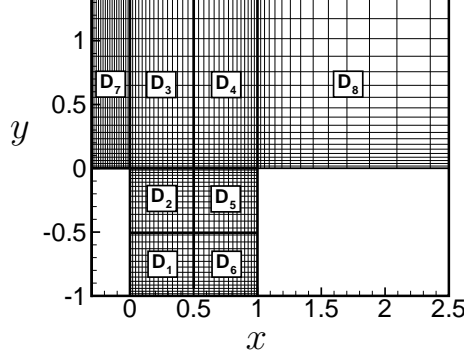


Figure 30: The partition \mathcal{P}_8 associated with the open cavity flows is displayed. Every six meshes are plotted in each direction with respect to mesh 1.

6.4. Influence of domains decomposition

In the following section, the mesh 1 is considered and $\beta = 24$. The reference values are associated with the full domain analysis based on the algorithm depicted in **Algorithms** b) and \mathcal{P}_4 . Two partitions of \mathcal{D} are analyzed, referenced as \mathcal{P}_4 and \mathcal{P}_8 corresponding to 4 and 8 subdomains respectively. The snapshots are performed on each subdomain, derived from a linearized DNS for \mathcal{P}_4 and \mathcal{P}_8 . The domains \mathcal{D}_i with regards to \mathcal{P}_4 and \mathcal{P}_8 are shown in Figures 22 and 30 respectively. Errors $-\log_{10}(e_r)$ in each subdomain for \mathcal{P}_4 and \mathcal{P}_8 are illustrated in Figure 31 with respect to modes 2 and 4. Regarding \mathcal{P}_4 , we observe that within the subset composed of \mathcal{D}_3 the error is minimized. It is physically relevant because spatial supports associated with modes 2 and 4 are mainly concentrated inside \mathcal{D}_3 . However, it is also surprising to notice that the unsteadiness is also well captured in \mathcal{D}_1 , \mathcal{D}_2 and \mathcal{D}_4 . In particular, the error is lower than the precision of the numerical method as estimated in the previous section. From these encouraging results, the partition \mathcal{P}_8 is now investigated, where the subdomain \mathcal{D}_3 is divided into 4 subdomains. Results are reported in Figure 31 e),f),g),h). It is interesting to note that errors with respect to \mathcal{D}_i which belong to \mathcal{P}_8 , do not increase compared to those of \mathcal{P}_4 . Consequently, the partitioning does not affect the linear dynamics. The eigenfunctions with regards to \mathcal{P}_4 and \mathcal{P}_8 computed from the algorithm based on subdomains **Algorithms** a) are shown in Figure 32. One may remark that the full spatial support is well recovered from the

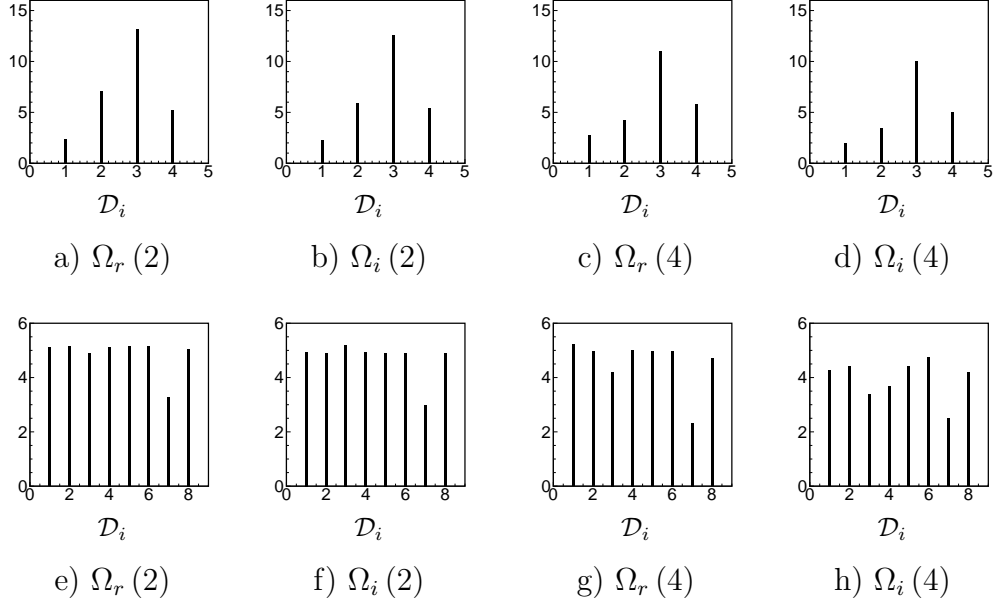


Figure 31: Error $-\log_{10}(e_r)$ analysis according to each subdomain with respect to partitions \mathcal{P}_4 and \mathcal{P}_8 and modes 2 and 4.

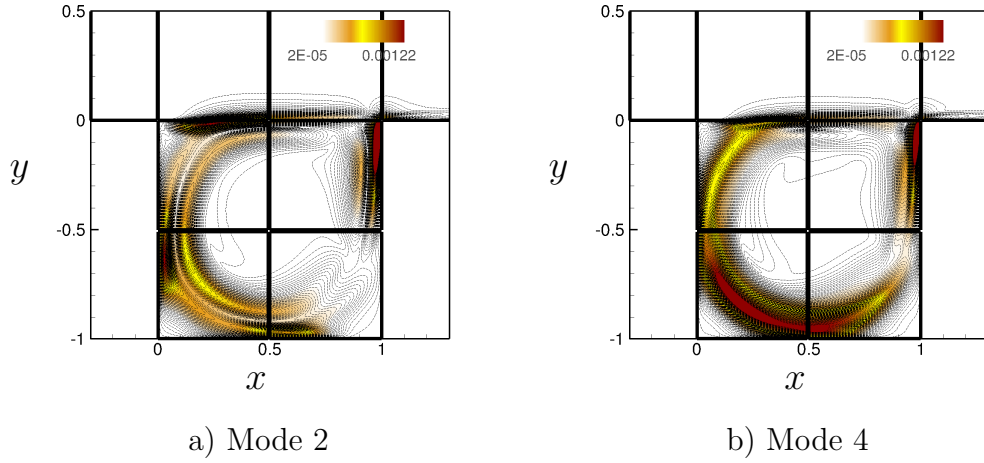


Figure 32: The spanwise perturbation velocity fields $|\hat{w}_r|$ is plotted with respect to modes 2 and 4 according to \mathcal{P}_4 (in flood) and \mathcal{P}_8 (in dashed lines).

partitions \mathcal{P}_4 and \mathcal{P}_8 . Similar observations could be established for modes 1 and 3.

7. Conclusions and prospects

This survey revisits a matrix-free method devoted to the global linear stability analysis based on a multidomains Direct Numerical Simulation code. A continuity influence matrix technique is introduced to solve grid points lying on interfaces between subdomains. A connectivity table is used to manage communication between each subdomain.

Through three benchmark problems, the lid-driven cavity flow and two open flows: the square cylinder and the open-cavity flows, it is demonstrated that no loss of accuracy occurs when the entire computational domain is partitioned into several subdomains.

Furthermore, extracting global modes provided from snapshots based merely on a subset of the entire flow field appears to not induce errors superior to the scheme precision. Moreover, it reproduces adequately the entire perturbation velocity fields by means of the connectivity table.

This is quite encouraging in terms of reducing the storage requirement associated with large computational domains. This method may also be of great interest to avoid contamination of global modes by boundary conditions, compared to a matrix method. Moreover, the multidomains strategy seems to be a natural way to exploit parallel architectures. In particular, the fact that we use the same partition with regards to the linearized DNS and the Arnoldi procedure should be useful to couple both algorithms. An implicitly restarted Arnoldi method relying on subspace iterations, similar as the one developed in ARPACK (Lehoucq et al. (1998)), could improve the efficiency of the global numerical method, for instance.

In addition, further developments dealing with curvilinear geometries by means of a coordinate transformation are also in progress.

Finally, our objective aims to simulate and extract three-dimensional flow dynamics in both linear and nonlinear regime of multi-connected rectangular domains based on three-dimensional periodic base flows. Preliminary work about the second bifurcation of a flow passing over an open cavity is in progress. Moreover, our matrix-free method combined with a Koopman modes solver (see Schmid (2010)) seems to be a promising tool to deal with spectral analysis according to three-dimensional nonlinear dynamics. Note

that a first attempt by considering the nonlinear regime of an open cavity flow within a two-dimensional framework has been recently addressed by Alizard et al. (2010c).

Acknowledgments

This work has received support from the National Agency for Research on reference BLAN08 – 1.309235. Computing time was provided by "Institut du Développement et des Ressources en Informatique Scientifique (IDRIS)-CNRS".

8. Appendix A: irregular staggered compact finite difference scheme validation

Numerical validations of the single-domain solver are reported in Chicheportiche et al. (2008) for a 2-D lid-driven cavity at Reynolds 1000. The same configuration is used to investigate the accuracy of the formulation developed for non uniform grids. In Tables 6 to 8, the values of the intensity of the primary, lower left secondary, and lower right secondary vortices respectively are compared to selected results of the litterature. The spectral simulations of Botella and Peyret (1998) constitute the reference. Compared to other numerical strategies, the present results are closer to the spectral reference for a given mesh size. The accuracy is also demonstrated by the comparison of the extrema of the vertical velocity through the centerlines of the cavity in Table 8, and in Figure 33. The L_1 -norm of the error with respect to Botella and Peyret (1998) is significantly reduced when using a Cartesian grid clustered near the walls with a geometric rate of 1 to 3%. The best results are obtained with a rate of 3%, and at least a second-order accuracy is obtained with the most defavorable choice for the mesh spacing (the minimum value), which is the leading order expected since the viscous term are discretized with second-order formulas (and obtained for instance for regular meshes).

Reference	Grid	ψ	ω	x	y
regular	N=30	0.104367	1.840809	0.4758	0.5914
stretched 1%	N=30	0.105609	1.860462	0.4754	0.5876
stretched 2%	N=30	0.106859	1.878305	0.4749	0.5839
stretched 3%	N=30	0.108099	1.895117	0.4742	0.5805
stretched 4%	N=30	0.109306	1.911081	0.4736	0.5774
stretched 5%	N=30	0.110454	1.925981	0.4731	0.5748
regular	N=80	0.116086	2.026451	0.4699	0.5682
stretched 1%	N=80	0.116990	2.039080	0.4697	0.5672
stretched 2%	N=80	0.117639	2.047501	0.4696	0.5664
stretched 3%	N=80	0.118080	2.052503	0.4696	0.5658
regular	N=124	0.117733	2.050945	0.4695	0.5665
stretched 1%	N=124	0.118294	2.058227	0.4694	0.5659
stretched 2%	N=124	0.118602	2.061679	0.4694	0.5655
stretched 3%	N=124	0.118748	2.062602	0.4694	0.5652
regular	N=150	0.118119	2.056438	0.4694	0.5661
stretched 1%	N=150	0.118558	2.062005	0.4693	0.5656
stretched 2%	N=150	0.118762	2.064049	0.4693	0.5653
stretched 3%	N=150	0.118835	2.064000	0.4694	0.5651
regular	N=250	0.118653	2.063866	0.4693	0.5656
stretched 1%	N=250	0.118858	2.066264	0.4693	0.5653
stretched 2%	N=250	0.118899	2.066121	0.4693	0.5652
stretched 3%	N=250	0.118883	2.064558	0.4693	0.5651
Botella and Peyret (1998)	N=64	0.1189365	2.068016	0.4692	0.5652
Botella and Peyret (1998)	N=160	0.1189366	2.067753	0.4692	0.5652
Barragy and Carey (1997)	257×257	0.118930	-	-	-
Schreiber and Keller (1983)	100×100	0.11315	1.9863	-	-
Schreiber and Keller (1983)	121×121	0.11492	2.0112	-	-
Schreiber and Keller (1983)	141×141	0.11603	2.0268	0.47143	0.56429
Schreiber and Keller (1983)	Extrapolation	0.11894	2.0677	-	-
Ghia et al. (1982)	129×129	0.117929	2.04968	0.4687	0.5625
Bruneau and Jouron (1990)	256×256	0.1163	-	0.4687	0.5586
Goyon (1996)	129×129	0.1157	-	0.4688	0.5625
Vanka (1986)	321×321	0.1173	-	0.4562	0.5625

Table 6: Intensities of the primary vortex, at Re= 1000; (x,y) refers to the center of the primary vortex, i.e. the location of the maximum value of the streamfunction.

Reference	Grid	ψ	ω	x	y
regular	N=30	-2.1590×10^{-3}	-1.064676	0.1585	0.1323
stretched 1%	N=30	-2.0640×10^{-3}	-1.054019	0.1554	0.1296
stretched 2%	N=30	-1.9689×10^{-3}	-1.046361	0.1519	0.1269
stretched 3%	N=30	-1.8879×10^{-3}	-1.041124	0.1485	0.1243
stretched 4%	N=30	-1.8279×10^{-3}	-1.041172	0.1457	0.1220
stretched 5%	N=30	-1.7883×10^{-3}	-1.044759	0.1434	0.1202
regular	N=80	-1.7322×10^{-3}	-1.084315	0.1379	0.1143
stretched 1%	N=80	-1.7342×10^{-3}	-1.093292	0.1374	0.1135
stretched 2%	N=80	-1.7349×10^{-3}	-1.099134	0.1369	0.1130
stretched 3%	N=80	-1.7347×10^{-3}	-1.103852	0.1366	0.1126
regular	N=124	-1.7330×10^{-3}	-1.099523	0.1369	0.1129
stretched 1%	N=124	-1.7328×10^{-3}	-1.104324	0.1365	0.1124
stretched 2%	N=124	-1.7322×10^{-3}	-1.106377	0.1362	0.1121
stretched 3%	N=124	-1.7315×10^{-3}	-1.109571	0.1361	0.1120
regular	N=150	-1.7325×10^{-3}	-1.102696	0.1366	0.1126
stretched 1%	N=150	-1.7313×10^{-3}	-1.107004	0.1361	0.1120
stretched 2%	N=150	-1.7319×10^{-3}	-1.108805	0.1363	0.1122
stretched 3%	N=150	-1.7307×10^{-3}	-1.109755	0.1360	0.1119
regular	N=250	-1.7311×10^{-3}	-1.101377	0.1362	0.1121
stretched 1%	N=250	-1.7304×10^{-3}	-1.108540	0.1360	0.1119
stretched 2%	N=250	-1.7300×10^{-3}	-1.109594	0.1360	0.1118
stretched 3%	N=250	-1.7297×10^{-3}	-1.110603	0.1359	0.1118
Botella and Peyret (1998)	N = 64	$-1.72968710 \times 10^{-3}$	-1.109714	0.1360	0.1118
Botella and Peyret (1998)	N = 160	$-1.72971710 \times 10^{-3}$	-1.109789	0.1360	0.1118
Ghia et al. (1982)		$-1.7510210 \times 10^{-3}$	-1.15465	0.1406	0.1094
Bruneau and Jouron (1990)		-1.9110×10^{-3}	-	0.1289	0.1094
Schreiber and Keller (1983)		-1.70010×10^{-3}	-0.9990	0.13571	0.10714
Goyon (1996)		-1.6310×10^{-3}	-	0.1329	0.1171
Vanka (1986)		-1.7410×10^{-3}	-	0.1375	0.1063

Table 7: Intensities of the lower left secondary vortex, at $Re = 1000$; (x,y) gives the location of the value of the streamfunction minimum.

Reference	Grid	ψ	ω	x	y
regular	N=30	-2.9669×10^{-4}	-0.325240	0.9187	0.0869
stretched 1%	N=30	-2.8784×10^{-4}	-0.329335	0.9182	0.0855
stretched 2%	N=30	-2.8186×10^{-4}	-0.335501	0.9176	0.0844
stretched 3%	N=30	-2.7804×10^{-4}	-0.342557	0.9169	0.0835
stretched 4%	N=30	-2.7571×10^{-4}	-0.349972	0.9163	0.0829
stretched 5%	N=30	-2.7429×10^{-4}	-0.355438	0.9159	0.0824
regular	N=80	-2.3852×10^{-4}	-0.350486	0.9164	0.0792
stretched 1%	N=80	-2.3805×10^{-4}	-0.352340	0.9164	0.0789
stretched 2%	N=80	-2.3795×10^{-4}	-0.353893	0.9164	0.0787
stretched 3%	N=80	-2.3814×10^{-4}	-0.354757	0.9165	0.0786
regular	N=124	-2.3524×10^{-4}	-0.351546	0.9166	0.0786
stretched 1%	N=124	-2.3519×10^{-4}	-0.352666	0.9166	0.0784
stretched 2%	N=124	-2.3537×10^{-4}	-0.353462	0.9166	0.0783
stretched 3%	N=124	-2.3572×10^{-4}	-0.353568	0.9166	0.0782
regular	N=150	-2.3461×10^{-4}	-0.351649	0.9166	0.0784
stretched 1%	N=150	-2.3464×10^{-4}	-0.352400	0.9167	0.0783
stretched 2%	N=150	-2.3484×10^{-4}	-0.353301	0.9166	0.0782
stretched 3%	N=150	-2.3521×10^{-4}	-0.353829	0.9166	0.0782
regular	N=250	-2.3384×10^{-4}	-0.351063	0.9167	0.0782
stretched 1%	N=250	-2.3392×10^{-4}	-0.352081	0.9167	0.0781
stretched 2%	N=250	-2.3413×10^{-4}	-0.352394	0.9167	0.0781
stretched 3%	N=250	-2.3454×10^{-4}	-0.352564	0.9166	0.0781
Botella and Peyret (1998)	N = 64	$-2.33453110 \times 10^{-4}$	-0.3521015	0.9167	0.0781
Botella and Peyret (1998)	N = 160	$-2.33452810 \times 10^{-4}$	-0.3522861	0.9167	0.0781
Ghia et al. (1982)		$-2.3112910 \times 10^{-4}$	-0.36175	0.9141	0.0781
Bruneau and Jouron (1990)		-3.2510×10^{-4}	-	0.9141	0.0820
Schreiber and Keller (1983)		-2.170010×10^{-4}	-0.30200	0.91429	0.07143
Goyon (1996)		-2.1110×10^{-4}	-	0.9141	0.0781
Vanka (1986)		-2.2410×10^{-4}	-	0.9250	0.0813

Table 8: Intensities of the lower right secondary vortex, at $Re = 1000$; (x,y) gives the location of the value of the streamfunction minimum.

Reference	Grid	v_{\max}	x_{\max}	v_{\min}	x_{\min}
regular	N=30	0.318276	0.8359	-0.448505	0.1041
stretched 1%	N=30	0.324279	0.8368	-0.457317	0.1040
stretched 2%	N=30	0.330001	0.8374	-0.465353	0.1031
stretched 3%	N=30	0.335452	0.8379	-0.472795	0.1019
stretched 4%	N=30	0.340621	0.8385	-0.479837	0.1005
stretched 5%	N=30	0.345454	0.8392	-0.486448	0.0988
regular	N=80	0.365800	0.8403	-0.512585	0.0930
stretched 1%	N=80	0.369489	0.8410	-0.517336	0.0923
stretched 2%	N=80	0.372150	0.8415	-0.520786	0.0918
stretched 3%	N=80	0.373974	0.8419	-0.523179	0.0914
regular	N=124	0.372238	0.8413	-0.520825	0.0917
stretched 1%	N=124	0.374525	0.8418	-0.523817	0.0913
stretched 2%	N=124	0.375799	0.8421	-0.525527	0.0910
stretched 3%	N=124	0.376430	0.8423	-0.526413	0.0908
regular	N=150	0.373744	0.8416	-0.522773	0.0915
stretched 1%	N=150	0.375542	0.8420	-0.525158	0.0911
stretched 2%	N=150	0.376392	0.8422	-0.526327	0.0909
stretched 3%	N=150	0.376729	0.8423	-0.526825	0.0908
regular	N=250	0.375834	0.8420	-0.525530	0.0910
stretched 1%	N=250	0.376682	0.8422	-0.526708	0.0908
stretched 2%	N=250	0.376879	0.8422	-0.527011	0.0908
stretched 3%	N=250	0.376883	0.8423	-0.527057	0.0907
Botella and Peyret (1998)	N=64	0.3769439	0.8422	-0.5270763	0.0908
Botella and Peyret (1998)	N=160	0.3769447	0.8422	-0.5270771	0.0908
Deng et al. (1994), cpi	128×128	0.37369	-	-0.52280	-
Deng et al. (1994), cpi	Extrapolation	0.37702	-	-0.52724	-
Deng et al. (1994), stagg.	128×128	0.36884	-	-0.51727	-
Deng et al. (1994), stagg.	Extrapol.	0.37705	-	-0.52690	-
Ghia et al. (1982)	129×129	0.37095	0.8437	-0.51550	0.0937
Bruneau and Jouron (1990)	256×256	0.3665	0.8477	-0.5208	0.0898

Table 9: Extrema of the velocity through the centerlines of the cavity, at Re= 1000.

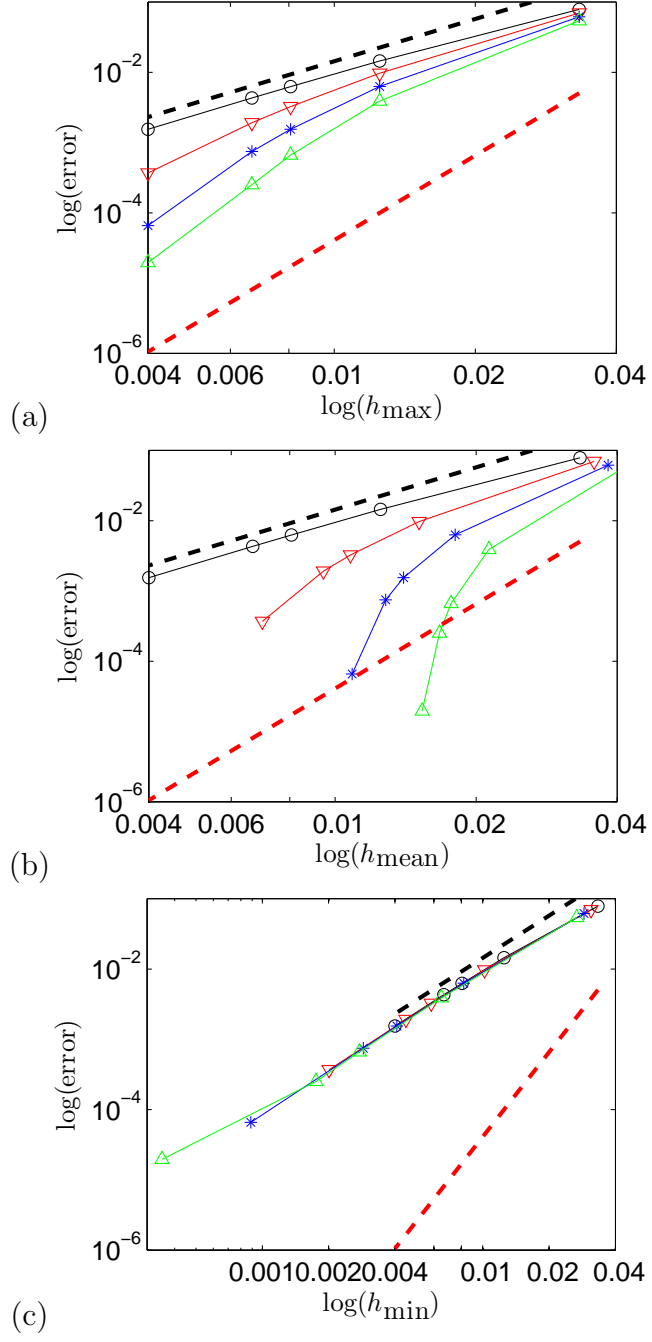


Figure 33: L_1 -norm of the error with respect to Botella and Peyret (1998) as a function of the maximum (a), average (b), and minimum value (c) of the mesh size: regular mesh The black and red broken lines indicate the second-order and fourth-order slopes respectively.

References

- Abide, S., Viazzo, S., 2005. A 2D compact fourth-order projection decomposition method. *J. Comput. Phys.* 206, 252–276.
- Åkervik, E., Brandt, L., Henningson, D., Hoepffner, J., Marxen, O., Schlatter, P., 2006. Steady solutions of the Navier-Stokes equations by selective frequency damping. *Physics of Fluids* 18, 068102.
- Åkervik, E., Hoepffner, J., Ehrenstein, U., Henningson, D., 2007. Optimal growth, model reduction and control in a separated boundary-layer flow using global modes. *J. Fluid Mech.* 579, 305–314.
- Alizard, F., Basley, J., Robinet, J., Faure, T., Gloerfelt, X., Pastur, L., Lusseyran, F., Delprat, N., 2010a. Flow dynamics in open square cavity: From linear instability to saturated regime. In: 8th Euromech Fluid mechanics conference, Bad Reichenhall, Germany, September 13-16.
- Alizard, F., Merle, X., Robinet, J.-C., Gloerfelt, X., 2010b. A domain decomposition matrix - free method for global linear stability. In: 40th AIAA Fluid Dynamics Conference and Exhibit, Chicago, USA, 28 June - 1 july.
- Alizard, F., Merle, X., Robinet, J.-C., Gloerfelt, X., June 30 – July 3 2010c. Linear and non-linear dynamics of a cavity flow. 8th Ercoftac Sig 33 Workshop - Global Instabilities of Open Flows Nice, France.
- Armfield, S., Street, R., 2003. The pressure accuracy of fractional-step methods for the Navier-Stokes equations on staggered grids. *Australian and New-Zealand Industrial and Applied Mathematics Journal* 44(E), C20–C39.
- Bagheri, S., Åkervik, E., Brandt, L., Henningson, D., 2009a. Matrix-free methods for the stability and control of boundary layers. *AIAA J.* 47, 1057–1068.
- Bagheri, S., Schlatter, P., Schmid, P., Henningson, D., 2009b. Global stability of a jet in crossflow. *J. Fluid Mech.* 624, 33–44.
- Barbagallo, A., Sipp, D., Schmid, P., 2009. Closed-control of an open cavity flow using reduced-order models. *J. Fluid Mech.* 641, 1–50.
- Barkley, D., Blackburn, H., 2008. Direct optimal growth analysis for timesteppers. *Int. J. For Num. Meth. in Fluids* 57, 1435–1458.

- Barkley, D., Gomes, G., Henderson, R., 2002. Three-dimensional instability in flow over a backward-facing step. *J. Fluid Mech.* 473, 167–190.
- Barkley, D., Henderson, R., 1996. Tree dimensional floquet stability analysis of the wake of a circular cylinder. *Journal Fluids Mech.* 322, 215–241.
- Barragy, E., Carey, G., 1997. Stream function-vorticity driven cavity solution using p finite elements 26, 453–468.
- Basley, J., Pastur, L., Lusseyran, F., Faure, T., Delprat, N., 2010. Experimental investigation of global structures in an incompressible flow using time-resolved piv. *Exp. Fluids* DOI: 10.1007/s00348-010-0942-9.
- Botella, O., Peyret, R., 1998. Benchmark spectral results on the lid-driven cavity flow 27, 421–433.
- Bres, G., Colonius, T., 2008. Three dimensional instabilities in compressible flow over open cavities. *J. Fluid Mech.* 599, 309–339.
- Breuer, M., Bernsdorf, J., Zeiser, T., Durst, F., 2000. Accurate computations of the laminar flow past a square cylinder based on two different methods: lattice-boltzmann and finite-volume. *International Journal of Heat and Fluid Flow* 21, 186–196.
- Brown, D., Cortez, R., Minion, M., 2001. Accurate projection method for the incompressible Navier-Stokes equations. *J. Comput. Phys.* 168, 464–499.
- Bruneau, C.-H., Jouron, C., 1990. An efficient scheme for solving steady incompressible Navier-Stokes equations 89, 389–413.
- Camarri, S., Iollo, A., 2010. Feedback control of the vortex-shedding instability based on sensitivity analysis. *Physics of fluids* 22, 094102.
- Chang, H.-R., Shirer, H., 1985. Compact spatial differencing techniques in numerical modeling. *Mon. Wea. Rev.* 113, 409–423.
- Chang, K., Constantinescu, G., Park, S., 2006. Analysis of the flow and mass transfer processes for the incompressible flow past an open cavity with a laminar and a fully turbulent incoming boundary layer. *J. Fluid Mech.* 561, 113–145.

- Chiba, S., 1998. Global stability analysis of incompressible viscous flow. *J. Japan Society of Comp. Fluid Dynamics* 7, 20–48.
- Chicheportiche, J., Merle, X., Gloerfelt, X., Robinet, J.-C., 2008. Direct numerical simulation and global stability analysis of three-dimensional instabilities in a lid-driven cavity. *C. R. Méc., Acad. Sci. Paris* 336, 586–591.
- Daube, O., 1992. Resolution of the 2D Navier-Stokes equations in velocity-vorticity form by means of an influence matrix technique. *J. Comput. Physics* 103, 402–414.
- De Vicente, J., Rodriguez, D., Theofilis, V., Valero, E., 2011. Stability analysis in spanwise-periodic double-sided lid-driven cavity flows with complex cross-sectional profiles 43, 143–153.
- Deng, G., Piquet, J., Queutey, P., Visonneau, M., 1994. Incompressible flow calculations with a consistent physical interpolation finite volume approach 23, 1029–1047.
- Edwards, W., Tuckerman, L., Friesner, R., Sorensen, D., 1994. Krylov methods for the incompressible navier-stokes equations. *J. Comp. Phys.* 110, 82–102.
- Ehrenstein, U., Gallaire, F., 2005. On two dimensional temporal modes in spatially evolving open flows: the flat-plate boundary layer. *J. Fluid Mech.* 536, 209–218.
- Faure, T., Pastur, L., Lusseyran, F., Fraigneau, Y., Bisch, D., 2009. Three-dimensional centrifugal instabilities development inside a parallelepipedic open cavity of various shape. *Exp. Fluids* 47, 395–410.
- Feldman, Y., Gelfat, A., 2010. Oscillatory instability of a three-dimensional lid-driven flow in a cube. *Physics of fluids* 22.
- Gamet, L., Ducros, F., Nicoud, F., Poinso, T., 1999. Compact finite difference schemes on non-uniform meshes. Application to direct numerical simulation of compressible flows 29, 159–191.
- Ghia, U., Ghia, K., Shin, C., 1982. High-re solutions for incompressible flow using the Navier-Stokes equations and a multigrid method 48, 387–411.

- Goedheer, W., Potters, J., 1985. A compact finite difference scheme on a non-equidistant mesh 61, 269–279.
- Goyon, O., 1996. High-reynolds number solutions of Navier-Stokes equations using incremental unknowns. *Computer Methods in Applied Mechanics and Engineering* 130, 319–335.
- Kleiser, L., Schumann, U., 1980. Treatment of incompressibility and boundary conditions in 3d numerical spectral simulation of plane channel flows. Hirshel Editor, *Notes on Numerical Fluid Dynamics*, Proc 3rd CAMM conf 2, Vieweg.
- Knoll, D., Keyes, D., 2004. Jacobian-free newton-krylov methods: a survey of approaches and applications. *J. Comp. Physics* 193, 357–397.
- Lehoucq, R., D.C., S., Chao, Y., 1998. ARPACK users’ guide: solution of large-scale eigenvalue problems with implicitly restarted Arnoldi methods. SIAM.
- Lele, S., 1992. Compact finite difference schemes with spectral-like resolution 103, 16–42.
- Mack, C., Schmid, P., 2011. Global stability of swept flow around a parabolic body: features of the global spectrum. *J. Fluid Mech.* in press.
- Merle, X., A, F., Robinet, J.-C., 2010. Finite difference methods for viscous incompressible global stability analysis. *Computers & Fluids* 39, 911–925.
- Pauley, L., Moin, P., Reynolds, W., 1990. The structure of two-dimensional separation. *AIAA J.* 220, 397–411.
- Peyret, R., 2002. *Spectral methods for incompressible viscous flow*. Springer.
- Pozrikidis, C., 2001. A note on the regularization of the discrete poisson/neumann problem. *J. Comp. Phys.* 172, 217–223.
- Raspo, I., 2003. A direct spectral domain decomposition method for computation of rotating flows in a t-shape geometry. *Computers & Fluids* 32, 431–456.

- Rodriguez, D., Theofilis, V., 2009. Massively parallel numerical solution of the Biglobal linear instability eigenvalue problem using dense linear algebra. *AIAA J.* 47, 2449–2459.
- Saad, Y., 2003. Iterative methods for sparse linear systems. 2nd ed, SIAM, Philadelphia.
- Sabbah, C., Pasquetti, R., 1998. A divergence-free multidomain spectral solver of the Navier-Stokes equations in geometries of high aspect ratio. *J. Comput. Physics* 139, 359–379.
- Schmid, P., 2010. Dynamic mode decomposition of numerical and experimental data. *J. Fluid Mech.* 656, 5–28.
- Schreiber, R., Keller, H., 1983. Driven cavity flows by efficient numerical techniques 49, 310–333.
- Sipp, D., Marquet, O., Meliga, P., Barbagallo, A., 2010. Dynamics and control of global instabilities in open flows: a linearized approach. *Applied Mech. Reviews* 63, 030801.
- Tezuka, A., Kojiro, S., 2006. Tree-dimensional global linear stability analysis of flow around a spheroid. *AIAA J* 44, 1697–1708.
- Theofilis, V., 2003. Advances in global linear instability of nonparallel and three-dimensional flows. *Prog. in Aerospace Sciences* 39, 249–315.
- Theofilis, V., 2011. Global linear instability. *Annu. Rev. Fluid Mech.* 43, 319–352.
- Theofilis, V., Duck, P., Owen, J., 2004. Viscous linear stability analysis of rectangular duct and cavity flows. *J. Fluid Mech.* 505, 249–286.
- Tuckerman, L., 1989. Divergence-free velocity fields in nonperiodic geometries. *J. Comput. Physics* 80, 403–441.
- Tuckerman, L., Barkley, D., 2000. Bifurcation analysis for timesteppers. *Numerical Methods for Bifurcation Problems and Large-Scale Dynamical Systems*, New York 119, 543–466.
- Vanka, S., 1986. Block-implicit multigrid solution of Navier-Stokes equations in primitive variables 65, 138–158.